2017

Development and Application of a MODIS Inorganic Sediment Model during the 2016 Mississippi River Diversion in Lake Pontchartrain, Louisiana

Robert Lee Iles IV
Louisiana State University and Agricultural and Mechanical College, riles2lsu@gmail.com

DEVELOPMENT AND APPLICATION OF A MODIS INORGANIC SEDIMENT MODEL DURING THE 2016 MISSISSIPPI RIVER DIVERSION IN LAKE PONTCHARTRAIN, LOUISIANA

A Thesis

Submitted to the Graduate Faculty of the
Louisiana State University and
Agricultural and Mechanical College
in partial fulfillment of the
requirements for the degree of
Master of Science

in

The Department of Oceanography and Coastal Sciences

by
Robert Lee Iles IV
B.S., Louisiana State University, 2012
May 2017

ACKNOWLEDGMENTS

I extend sincerest gratitude to my advisor, Dr. Nan Walker, whose guidance and instruction throughout this process was integral to the project's successful completion and to my development as a scientist. She inspired me to explore new areas of research and was patient in instructing me when I did not at first understand new concepts. Dr. Walker's confidence in me was an inspiration, especially during the strenuous moments of this project. I am also thankful to Dr. Robert Rohli, who was not only helpful with this project, but has been a mentor throughout my graduate school career. Dr. Rohli is always quick to give advice and to provide corrections, and I am thankful for his continuous encouragement. I would also like to thank Dr. John White for providing the field data necessary for this project, for the generous use of his lab for further data analysis, and for his constructive advice on the final manuscript.

I am extremely grateful to Mr. Alaric Haag of the Earth Scan Laboratory, without whose technical expertise and patience in teaching me this project would have been impossible. Mr. Haag provided crucial help with image processing and additionally aided in my understanding of computer science concepts, both of which were not only essential to this project but will also give me an advantage in my career going forward. I owe special thanks to Mr. Ishan Joshi, who was also helpful with the image processing software as well as with field data collection and in helping me to understand some of the fundamental concepts of remote sensing.

I would also like to acknowledge Ms. Sarah Wood and Mr. Tommy Blanchard for their help in the field data processing portion of the project. Thank you to Mr. Eddie Weeks for donating his time to bring us to the field to collect data despite difficult driving conditions during the March 2016 floods. Additionally, I thank Ms. Cyndhia Ramatchandirane and the Water Institute of the Gulf for the generous use of their Barataria Bay field data.

Additional thanks to Dr. Lei Wang for his help in setting me on this path at the beginning of my graduate career. Also, thank you to Dr. Robert Carney, whose Introduction to Oceanography class in my very first undergraduate semester at LSU sparked my passion for oceanography.

I owe special thanks to Mr. Brant Mitchell for his generosity in allowing me to split time between work and school and his patience and understanding when school obligations required more of my attention. Also, thank you to Mr. Paco Capello for his continuous support and to Mr. Nick Robles for his help and friendship throughout my time at SDMI.

Thank you to Mrs. Anne Prendergast, whose lessons in strict attention to grammar have aided my writing abilities, even if it may have seemed I was not paying close attention. Thank you to Mrs. Kathey Groves, who preached, "If you write well, you will excel," and by whose reckoning I hope my words to have been well crafted. And thank you to Kathleen DesHotel, who afforded me more opportunities than I deserved and from whom I learned the importance of creativity and imagination in life and in writing, concepts that often are not discussed in science, but which I have found valuable still.

Thanks to my parents, who trained me up in the way that I should go and have helped me not to depart from it, and to my sisters. I am forever grateful for all of their love and provision throughout my life. I could not have been blessed with a more wonderful family.

To my wife, Bryanna, I am unable to articulate the full amount of my appreciation or my love. As iron sharpens iron, she has comforted me in stressful moments, strengthened me to persist through trials, and had faith in me when I had none. Without her, neither this project nor anything I do in life would be possible or worth it.

TABLE OF CONTENTS

LIST OF TABLES

LIST OF FIGURES

LIST OF ABBREVIATIONS

BCS	Bonnet Carré Spillway
CWP	Clear-water pixel
ISC	Inorganic sediment concentration
MODIS	Moderate-resolution imaging spectroradiometer
MSY	Louis Armstrong New Orleans International Airport
NIR	Near-infrared
OSC	Organic sediment concentration
SSC	Suspended sediment concentration

ABSTRACT

The Bonnet Carré Spillway (BCS) is a Mississippi River diversion located on the southwestern coastline of Lake Pontchartrain in Louisiana. The discharge of potentially high amounts of Mississippi River nutrients and sediments during BCS diversion events has a noted ecological impact on the Lake Pontchartrain estuary. Projected river flooding prompted the opening of the Spillway from 10 January to 1 February 2016. MODIS satellite imagery were aerosol-corrected and then compared to *in-situ* measurements of inorganic sediment concentration (ISC) to derive a predictive algorithm for estimating ISC (in mg L^{-1}) in Lake Pontchartrain for satellite images in January and February. The new sediment imagery allowed for enhanced observation of sediment plume morphology, areal distribution, and directional motion trends within the Lake.

The spatial area of sediment concentrations >50 mg L^{-1} and >100 mg L^{-1} within the Mississippi River sediment plume was calculated for 12 dates in January and February. The average Lake Pontchartrain ISC was calculated for 20 image dates. Results suggest that the sediment plume areal distribution was linked to BCS discharge rate in the early stages of the diversion event, while both wind speed and direction were potentially more impactful as the event progressed in time. The 50 mg L^{-1} plume area peaked on 23 January at ~1,117 km^2, 68% of total Lake Pontchartrain area, while the 100 mg L^{-1} plume's maximum distribution was observed on 29 January at which time its area was ~905 km^2, 55% of the Lake's total area. The sediment plume tended to be located along the southern coastline of Lake Pontchartrain and observed a general eastward motion, which was calculated to be ~1 km h^{-1} for the first week of the event. Periods of strong winds from 19 to 24 January, 7 to 8 February, and 18 to 25 February corresponded to significant increases in plume area and mean Lake ISC for those date ranges.

Similarly, reduced winds from 29 January to 5 February may explain observed decreases in plume area for that timeframe. Additionally, wind direction appeared to help determine the location of the areas of highest sediment concentration.

CHAPTER 1: INTRODUCTION

1.1 Background

The Bonnet Carré Spillway (BCS) is a part of an array of flood control structures that exist to mitigate potential disasters that can arise due to flooding of the Mississippi River in Louisiana. The spillway is situated on the eastern bank of the river about 30 km west of New Orleans and 80 km southeast of Baton Rouge (Figure 1.1), atop a former delta of the Mississippi River, the largest river delta in North America (Kolic et al. 2014). During times when the River's projected flood stage is deemed to pose an extreme risk of flooding, some or all of the 350 bays of the spillway are opened to divert a portion of the river's water into Lake Pontchartrain.

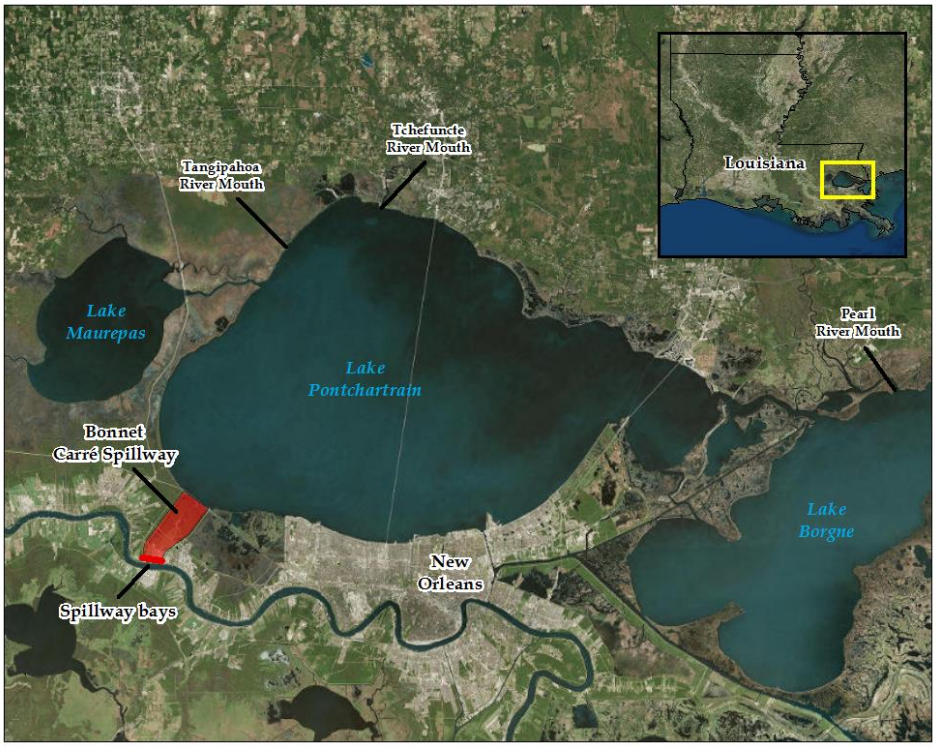

Figure 1.1: The Lake Pontchartrain Basin

The BCS was constructed in 1931 as a direct response to the Great Flood of 1927, an event which resulted in approximately 200 deaths and damages totaling over $200 million (Jadwin 1927). The spillway's primary objective is the protection of the greater New Orleans

area, which experienced some flooding in 1927 but was largely spared because of the deliberate breaching of the levee in other areas. The BCS has been opened eleven times since its construction, of which five instances (in 1945, 1950, 1973, 1979, and 1983) involved opening all 350 bays. By all accounts, the BCS has been an effective flood mitigation strategy for the New Orleans area.

As with most major human-environment interactions, the opening of the BCS has had unintended impacts and consequences. While the opening of the BCS reduces flood concerns for metropolitan New Orleans and adjacent areas downriver, the spillway also introduces a large amount of fresh water and sediments into Lake Pontchartrain. This rapid influx of fresh water into the usually brackish environment of Lake Pontchartrain can disrupt the vitality of fauna, such as blue crabs, which tolerate only a specific range of salinity (Ogburn et al. 2007). Furthermore, submerged aquatic vegetation, which provides an important food source for many commercially and ecologically important fauna, is harmed by the increase in water turbidity, owing in part to the increased sediment flow from the spillway (McCorquodale et al. 2009). As the turbidity increases, the amount of photosynthetically available radiation from sunlight decreases, thus reducing the productivity of such vegetation.

The addition of nutrients to the Pontchartrain Basin via the spillway can also have a profound impact on the estuarine system. Rapidly increasing nitrogen concentrations may result in phytoplankton blooms, which often result in a reduction in dissolved oxygen (Goolsby and Battaglin 2001). Phytoplankton blooms also have the potential to harm the health of both humans and marine fauna through ingestion of phytoplankton-produced biotoxins (de Magalhaes et al. 2001, Costa 2016, Manganelli 2016). Studies have observed harmful algal blooms of

cyanobacteria occurring after previous openings of the BCS in 1997 (Turner et al. 2004) and 2008 (Bargu et al. 2011), but not during the 2011 event (Roy et al. 2013).

The dispersal direction, speed, and fate of Mississippi River water and sediments in the lake during a diversion event are important in understanding the degree and location of impact to the system. The prevailing direction and magnitude of the wind, the amount of rainfall preceding the opening of the spillway, local river inputs, coastal water levels, and the seasonal climatology, especially the prevailing wind direction, all influence whether sediments linger in the lake suspended, sink, or exit swiftly toward Lake Borgne and, ultimately, the Gulf of Mexico. Given that different numbers and locations of spillway bays are opened in different flood events, and given the different antecedent and concurrent environmental conditions associated with each BCS opening, the BCS's influence on the Pontchartrain Basin differs each time it is opened. Understanding the impacts of BCS openings can be greatly enhanced by the use of remotely-sensed imagery.

1.2 Review of NASA Satellite-Based Ocean Remote Sensing Sensors

Monitoring of aquatic systems from space was first made possible by the NASA TIROS-1 satellite in 1960 which used television cameras to take snapshots of cloud cover and the Earth's surface (National Oceanic and Atmospheric Administration (NOAA) 2016). Satellite technology has since evolved to the extent that ocean variables such as sea surface temperature, suspended sediment concentrations, phytoplankton chlorophyll *a*, primary productivity, salinity, and other variables can be observed through analysis of the spectral signatures comprising a satellite image. Different components of the oceanic or coastal system absorb or reflect light only at specific and consistent wavelengths. Observations of the degree of absorption or reflection at various spectral wavelengths provide researchers, policymakers, and community managers the

ability to make quick decisions about the condition of the sea in the absence of ground truth measurements. Often the spectral reflectance at wavelengths of interest in such imagery is enhanced or altered digitally, especially by the use of colors, in order to accentuate the features of interest for ease in interpretation.

The world's first ocean color sensor was NASA's Coastal Zone Color Scanner (CZCS) which was launched in 1978 (Hovis et al. 1980) and ceased operation in 1986. The CZCS was initially intended as a simple "proof-of-concept" of the merits of visible band satellite remote sensing (International Ocean Colour Coordinating Group (IOCCG) 1999; Antoine et al. 2003). Although the CZCS only acquired data in six spectral bands (IOCCG 2014a), a low number in comparison to its successors, the mission proved to be revolutionary in the field of oceanography (Barber and Hilting 2000).

The successes of the CZCS mission prompted the development of new and more robust ocean color remote sensing satellite sensors. In 1997, the Sea-viewing Wide Field-of-view Sensor (SeaWiFS) was launched and it remained in operation until 2010. Although the spectral resolution of eight spectral bands exceeded that of CZCS, the SeaWiFS spatial resolution of 1100 m was coarser than the 825 m resolution of CZCS (IOCCG 2014b). SeaWiFS was initially designed solely for the measurement of phytoplankton chlorophyll *a* and primary productivity, but it was eventually calibrated to measure terrestrial plant life as well (Lynch 2011).

Two moderate-resolution imaging spectroradiometer (MODIS) sensors were launched aboard separate satellites, Terra and Aqua, in 1999 and 2002, respectively, each acquiring spectral data across 36 identical bands (Barnes et al. 1998). The satellites were designed such that Terra travels southward and Aqua northward relative to the equator during daytime, providing morning and afternoon images, respectively, and comprehensive synoptic views of

Earth's surface every one to two days. Both Terra and Aqua are still functional at the time of this writing. Table 1.1 compares the MODIS sensor specifications to the other two NASA sensors discussed.

Table 1.1: Comparison of three NASA ocean color sensors

Sensor	Bands	Spatial Resolution
CZCS	6	825 m
SeaWiFS	8	1100 m
MODIS	36	250 m (bands 1-2), 500 m (bands 3-7), 1000 m (bands 8-36)

In both satellite and ground-truthing oceanographic applications, an important method of classifying ocean regions ecologically and optically is the designation of areas as Case 1 or Case 2 waters. Case 1 waters, usually offshore, are those wherein the observed optical variability is dominated by the effects of phytoplankton pigments, primarily by the pigment chlorophyll *a*. By contrast, Case 2 waters are usually in areas nearer to the coastline, where inorganic particles, such as clay, silt, and sand, as well as organic detrital particles and colored dissolved organic matter (CDOM), can overshadow the optical variability due to phytoplankton pigments (Morel and Prieur 1977). The generally stable conditions of Case 1 waters make remote sensing algorithm development for those waters easier and more applicable to the global ocean. Case 2 waters, however, typically require more complex algorithms to characterize the relationship between in-water substances and satellite reflectance, even in different bays or estuaries of the same coastal regions. Case 2 water constituents are highly variable in time and from place to place. The quantification of these constituents is of special concern because of their heightened impact upon the more active coastal ecosystems and their potential to influence human health and the economy. The imagery acquired from the aforementioned satellite sensors must therefore be analyzed differently for Case 2 waters by comparing satellite data to *in-situ* data from the study region in question. The methods of processing imagery involve complex atmospheric and

aerosol correction algorithms, the latter of which cannot be as easily standardized for Case 2 waters.

1.3 Study Area and Timeframe

1.3.1 Mississippi River

The Mississippi River and its tributaries, covering an area of approximately 41% of the continental U.S., comprise the fourth largest watershed in the world (Elliot, 1932). The Mississippi River is economically vital to the United States as it provides a means of transportation to a number of large cities situated along the length of the river, but it also presents challenges for communities who depend on the river.

Much of the land that is drained into tributaries of the Mississippi or the Mississippi itself is used for agricultural activity. Runoff, from agricultural areas, flows into the Mississippi River and eventually the Gulf of Mexico. Nitrogen and phosphorus used in chemical fertilizers are of special concern because of their link to hypoxia in Gulf of Mexico waters of coastal Louisiana (Turner and Rabalais, 1991; Justic et al., 1993; Turner and Rabalais, 1994; Burkart and James 1999).

Repeated flooding of the Mississippi River, either due to extreme rain events or snowmelt runoff, has caused a number of disasters over the years. The costliest and deadliest Mississippi River disaster was the Great Flood of 1927. Although flood control measures like simple earthworks levees were already in place by that time, the 1927 flood prompted the enhancement of the levee system and the construction of more robust flood control structures.

1.3.2 Bonnet Carré Spillway

In response to the Great Mississippi River Flood of 1927, the United States Army Corps of Engineers began to strategize flood control measures to protect New Orleans and the

surrounding areas from future Mississippi River flood events. By 1928, the "Jadwin Plan" was devised and construction of a large diversion, the BCS, began in an area about 50 km west of New Orleans. Construction of the spillway was completed by 1931 (Barry 1997).

Each of the 350 bays, or "doors," of the BCS is six meters long. At its peak discharge, the Spillway can divert up to 7,079 $m^3 s^{-1}$ of the Mississippi River's water into Lake Pontchartrain (USACE 2016). When the river begins to approach its flood stage of 5 meters at New Orleans, the US Army Corps of Engineers decides whether to open some or all of the bays of the spillway. The amount of Mississippi River water that enters the lake thereafter depends on the number of bays that have been opened. While the bays control the volume of Mississippi River water that is allowed into the lake, the amount of total sediment or nutrients that enter is a function of other factors including input from northern Lake Pontchartrain tributaries, wind, and timing of the event (White et al. 2009; Roy et al. 2013).

1.3.3 Lake Pontchartrain

Encompassing an approximate area of 1,637 km^2, Lake Pontchartrain (Figure 1.2) is the largest lake in Louisiana and the eleventh largest in the United States although it more closely fits the technical definition of an estuary. The lake's water is typically brackish, with a salinity averaging between 1 and 6 ppt (McCorquodale et al. 2009) and as high as 8 ppt in some years (Sikora and Kjerfve 1985) and varying with distance from land. The most important factor regulating salinity in Lake Pontchartrain is tributary river discharges, specifically those of the Amite, Tickfaw, Natalbany, Tangipahoa, Tchefuncte, as well as other smaller bayous and streams. Additionally, although the Pearl River does not flow directly into the Lake itself, when its total discharge is increased, it is sufficient to restrict the higher-salinity Gulf of Mexico waters from entering Lake Pontchartrain (Sikora and Kjerfve 1985).

Figure 1.2: The Bonnet Carré Spillway's location in the Lake Pontchartrain Basin

The Lake Pontchartrain Basin encompasses over 26,000 km^2 including the land areas bordering Lakes Pontchartrain, Maurepas, and Borgne, in addition to their surrounding estuaries and the lakes themselves (LPBF 2016). Commercial fishing within this area accrued over $70 million in 2013 alone (Barnes et al. 2016), which strengthens the local economy. Additionally, coastal Louisiana, including the Lake Pontchartrain Basin, is acknowledged as an important tourist destination; recreational tourism in the Louisiana coastal area in 2012 accounted for an estimated 1.2 million visitors per year and generated $29 million in self-generated revenue (Barnes et al. 2015).

1.3.4 Recent Mississippi River Floods

The three most recent openings of the BCS, prior to the 2016 event, occurred in 1997, 2008, and 2011. The 1997 opening took place from 17 March to 17 April; in 2008 the spillway was open from 11 April to 8 May; and in 2011 the spillway was open from 9 May to 20 June.

The 2011 event had nearly two times the total spillway water discharge of the 1997 event and three times that of the 2008 event. Additionally, the 2011 event was double the 2008 event in total freshwater plume area (Roy et al. 2013). The overall ecological response to each BCS event varies based on factors including, but not limited to, the total size and volume of the Mississippi River plume; discharge from northern tributaries including the Tchefuncte, Amite, Tickfaw, Pearl, and Tangipahoa Rivers; timing of the event; and sustained wind speed and direction (Roy et al. 2013).

1.3.5 2016 Mississippi River Flood

Heavy rains throughout the Mississippi River watershed in early 2016 prompted the opening of the BCS from 10 January to 1 February. At its peak, 210 of the structure's 350 bays were opened during the event. The timing of the 2016 event was unique in that it was the earliest ever opening in a year; the next earliest was the 1937 opening, which occurred from 28 January to 16 March of that year. Most previous BCS openings took place in the spring or summer months from March to June, so the timing of this event was unique.

1.4 Research Objectives and Key Questions

The main objective of this study was to determine the degree to which the 2016 BCS diversion event impacted the sediment regime of Lake Pontchartrain. The research primarily focused on Lake Pontchartrain proper, the largest water area of the Lake Pontchartrain Basin. Analysis of suspended sediment concentrations (SSC), inorganic sediment concentrations (ISC), and organic sediment concentrations (OSC) from field data collections before, during, and after the diversion event, coupled with satellite imagery and field collections of spectroradiometer data, were used to develop a predictive regression model for precise mapping of the time history of several surface sediment plume characteristics; including distribution and area, sediment

concentration, and motion. Wind speed and direction were investigated as forcing factors for the plume characteristics over time. The key questions that were answered by this research are:

1. Is the clear-water pixel (CWP) method an effective technique for aerosol correction in Lake Pontchartrain?
2. Using *in-situ* sediment data and the CWP method for aerosol correction, can a predictive model for Lake Pontchartrain sediment concentration be derived?
3. Can the regression model developed in (2) be used to the approximate the concentration and spatial distribution of the Mississippi River sediment plume from the 2016 BCS diversion?
4. What impact did the wind speed and direction have on the plume characteristics as revealed in the time history of MODIS imagery?
5. Although the satellite reflectance data only yields a near-surface measurement, can it reveal the fate of the new sediment within the lake?

1.5 Thesis Structure

Chapter 2 provides a summary of literature pertaining to the fundamentals of remote sensing research, how such research can be used for sediment-related study in coastal Louisiana, as well as a brief discussion on the potential significance of Mississippi River water to Lake Pontchartrain. Chapter 3 outlines the relevant data that was collected. Chapter 4 presents both the methods and the results of the aerosol correction methodology applied to all MODIS satellite imagery. Chapter 5 employs the aerosol correction results of Chapter 4 to perform an aerosol correction upon the imagery for which "ground truth" field measurements were collected. These imagery are used in the creation of a new predictive sediment algorithm. Images detailing inorganic sediment concentration were then created using the results from both Chapters 4 and 5.

The new sediment imagery allows for the characterization of the Mississippi River sediment in Lake Pontchartrain, which is presented in Chapter 6. Chapter 6 also contains a discussion on the potential meteorological, oceanographic, and physical forcing factors for the observations made about the time history of sediment plume morphology and concentration. Finally, Chapter 7 concludes the project, responds to the research objectives put forth in Chapter 1, and suggests ways in which remote sensing methods could be improved upon for similar research topics in the future.

CHAPTER 2: LITERATURE REVIEW

The Mississippi River plays a pivotal role in the ecology of coastal Louisiana, including Lake Pontchartrain. The Mississippi River and its tributaries drain nearly 41% of the United States and the river is the dominant source of freshwater discharge and nutrient load to the northern Gulf of Mexico by way of the bird-foot delta in southeast Louisiana (Eadie et al. 1994). As human activity increases along the Mississippi River's banks, so too does the amount of byproducts from such activities that enter the river's waters. Some of the sources of nutrients that enter the Mississippi River include sewage treatment, agriculture, and municipal and industrial runoff (Howarth et al. 2002). The influx of increasing amounts of nutrients has played a large role in eutrophication of the northern Gulf of Mexico, especially along the coast of Louisiana, which has subsequently resulted in pronounced ecological effects on these systems (Turner and Rabalais 1991). Freshwater river discharge also results in stratification of the water column, which compounds the problems of eutrophication (Rabalais et al. 1991; Wiseman et al. 1997).

One of the most efficient methods for continuous, long-term monitoring of the health of Louisiana's coastal ecosystem is via satellite remote sensing. In this chapter, the principles and techniques of ocean remote sensing are presented with a special emphasis on its usage for monitoring suspended sediment concentration (SSC) in the Lake Pontchartrain Basin.

2.1 Ocean Remote Sensing Overview

Ocean remote sensing involves the measurement of the surface upwelling radiance at various wavelengths ranging from the visible to infrared and longer wavelengths. Instruments used in ocean remote sensing can be handheld devices, shipborne or airborne devices, or earth-orbiting satellites. Satellite sensors measure top of atmosphere (TOA) radiance, which includes more than the water surface radiance. Satellite-derived remote sensing data can only be

practically applied for research or monitoring purposes after processing to remove non-water radiance sources. Additionally, understanding the individual reflectance spectra of various water constituents provides the ability to quantify different processes in the ocean including, but not limited to, chlorophyll *a* pigment analysis (Hu et al. 2000; Walker and Rabalais 2006; Wang et al. 2010) and other phytoplankton pigments (Dash et al. 2011), sea surface temperature (Walker et al. 2003), coastal land extent changes (Allen et al. 2012), or the tracking of oil spills (Walker et al. 2011). In order to comprehend how ocean remote sensing can be used for these and other applications, the underlying theories of remote sensing must first be understood.

The principal sources of radiation measured by passive satellite sensors, (i.e., those which only receive light/energy, as opposed to active sensors which deploy and subsequently receive light/energy) such as MODIS, are reflected solar radiation (visible and near-infrared (NIR)) and near-black body emitted radiation (mid-IR and thermal-IR). Emissivity (ε) describes the degree to which a surface emits and absorbs energy. A more reflective surface has a lower emissivity. A "black body" both absorbs and emits energy with perfect efficiency and, therefore, has an emissivity of 1. A "white body" is a perfect reflector and has an emissivity of 0, while a "grey body" is any surface whose emissivity is between 0 and 1. Both the sun and water act as hypothetical black bodies with the emissivity of water equal to approximately 0.98, depending upon the wavelength. Emissivity values of a surface are highest when the surface is viewed from nadir; reduction of the viewing angle reduces emissivity. Additionally, emissivity of water is greatly reduced in the microwave portion of the spectrum (Robinson 2004).

The measure of solar radiation that reaches a surface is expressed as radiant flux (Φ), which is the rate of solar energy (Q) flow through time (t):

$$\Phi = \frac{dQ}{dt}$$

The radiant intensity (I), expressed as W sr^{-1}, is the radiant flux per solid angle (ω) in a given direction:

$$I = \frac{d\Phi}{d\omega}$$

Radiant intensity is needed for the calculation of spectral radiance (L), which, in addition to irradiance (E), is ultimately used in the calculation of remote sensing reflectance. Spectral radiance, expressed in units W sr^{-1} m^{-2} nm^{-1}, is a function of radiant intensity per unit projected source area (A), written as

$$L = \frac{dI}{d(A \cos \theta)}$$

where θ is the angle between the propagated radiant flux direction and the azimuth angle (Robinson, 2004).

In ocean remote sensing, the amount of radiance that is ultimately measured by a satellite sensor is a composite of atmospheric scattering, sunglint, and water-leaving radiance. As much as 90% of the measured radiance can be due to atmospheric scattering (Robinson 2004) with most of that scattering being a result of Rayleigh scattering by air molecules and Mie scattering by aerosols (Gordon 1978). Mie scattering can include smoke, dust, volcanic material, and haze. Assuming the contribution by sunglint to be negligible, Robinson (2004) expressed radiance (L) as the sum of Rayleigh scattering by air molecules (L_r), Mie scattering by aerosols (L_a), and water leaving radiance (τL_w), or

$$L = L_r + L_a + \tau L_w$$

where τ is the diffuse transmittance of photons from different regions adjacent to the desired field of view (FOV).

Irradiance, expressed in units of W m^{-2}, is the measure of radiance arriving at the surface (Robinson 2004). Irradiance is used in the calculation of subsurface irradiance reflectance (R)

$$R = \frac{E_u}{E_d}$$

where E_u is the upwelling irradiance and E_d is the downwelling irradiance. The sum of reflectance and emissivity is always equal to 1. The ratio of upward water-leaving radiance (L_w) and the downwelling irradiance (E_d) is the remote sensing reflectance (R_{rs}):

$$R_{rs} = \frac{L_w}{E_d}$$

Remote sensing reflectance is expressed in units of sr^{-1}. "R" and "R_{rs}" are apparent optical properties (AOPs) of the water mass.

The amount of upwelling or downwelling light in the instantaneous field of view is a function of the amount of scattering or absorption taking place within the near-surface water column at the moment of observation. The inherent optical properties (IOPs) of pure seawater and its constituents are not measurable by satellite sensors and do not differ under different light conditions, but do vary within a water mass. IOPs, including the absorption coefficient (a) or backscattering coefficient (b), describe the degree to which water and its constituents are responsible for absorption or scattering. In ocean color remote sensing, the five main variables responsible for changes in absorption and/or backscattering are phytoplankton, colored dissolved organic matter (CDOM), suspended inorganic sediments (e.g., sand, silt, or clay), non-algal particles including suspended organic sediments, and water itself. Increased backscatter results in an increase in reflectance while increased absorption reduces reflectance (Robinson 2004).

The total absorption coefficient (a) reflects the overall absorption by water (a_w), phytoplankton (a_{ch}), non-algal particles (a_{os}), and CDOM (a_{ys}):

$$a = a_w + a_{ch} + a_{os} + a_{ys}$$

The total scattering coefficient (b) is the sum of scattering by water (b_w), phytoplankton (b_{ch}), and suspended inorganic sediment particulates (b_{is}):

$$b = b_w + b_{ch} + b_{is}$$

AOPs, such as the diffuse (or irradiance) attenuation coefficient ($K_\lambda(z)$ at wavelength λ and depth z) or the aforementioned subsurface irradiance reflectance (written as $R_\lambda(z)$ at wavelength λ and depth z), are derived from the IOPs of the water column which they describe and the specific light conditions affecting that water column at the time of observation. The diffuse attenuation coefficient can be expressed as

$$K(\lambda) = -E^{-1}(\lambda, z)\frac{dE}{dz}$$

where K is either downwelling or upwelling, depending on whether E_d or E_u is used in place of 'E' in the above equation.

Radiative transfer theory seeks to define how the subsurface light field is affected by the IOPs of water and the light propagation angle. The underwater light field can be modeled numerically through the use of Monte Carlo methods which simulate the behavior of a large number of photons in order to derive AOPs as a function of IOPs (Gordon et al. 1975). However, these Monte Carlo approaches are complex and require detailed knowledge of the IOPs and their spectral distribution, which is difficult to acquire (Robinson 2004). Despite these complications, some modeling studies of radiation transfer have provided the ability to simulate the subsurface light field as a function of absorption and backscattering. As previously noted, irradiance

reflectance (R) depends on the ratio between the absorption coefficient (a) and the backscattering coefficient (b). A modeling study by Morel and Prieur (1977) expressed reflectance as

$$R = 0.33\frac{b}{a}$$

which is a useful scenario for most ocean applications, wherein the b:a ratio is less than 0.3 (Robinson 2004). Morel and Prieur's (1977) study was based upon research by Gordon et al. (1975) which showed reflectance to be

$$R = 0.33\left(\frac{b}{a+b}\right)$$

In another example, Morel and Gentili (1993) define reflectance as

$$R = f\left(\frac{b}{a}\right)$$

where 'f' is a variable, usually between 0.3 and 0.5, that is itself a function of the sun angle.

These equations simply illustrate how IOPs influence AOPs, specifically how reflectance is impacted by the absorption to backscatter ratio. However, low absorption does not necessarily result in increased reflectance if there are no backscattering constituents within the water. Thus, both clear water and turbid water containing much absorbing material could have equally low reflectance values (Robinson 2004). This principle is especially important to consider for the 2016 BCS diversion event because the method used for aerosol correction is dependent on the assumption that little organic matter or CDOM was present to absorb light at red and near-infrared (NIR) wavelengths. This assumption was substantiated by this project's *in-situ* data analysis as discussed in Chapters 3 and 4.

2.1.1 Atmospheric and Aerosol Correction

Visible band ocean remote sensing applications require an empirical isolation of the water-leaving radiance (L_w) value in order to calculate remote sensing reflectance (R_{rs}) and, in turn,

provide insight into the makeup of the water's constituents. This process is termed "atmospheric correction." Atmospheric correction is a necessary step in remote sensing in order to remove the effects of Rayleigh scattering by the atmosphere. Gordon (1978) estimates that a 10% error in determining radiance, through inaccurate atmospheric correction, results in a 50% error in the calculation of reflectance, which in turn leads to incorrect calculations of ocean constituents. While sunglint must be considered in the overall correction schema, some sensors (e.g., SeaWiFS, CZCS) have the capability of tilting to minimize the effects of sunglint contamination. The MODIS sensors were designed without a tilting mechanism and, thus, sunglint-contaminated imagery is often a problem. However, such flawed imagery is usually identifiable by the naked eye and can be discarded. Unfortunately, the frequent presence of clouds in coastal Louisiana imagery, as well MODIS sunglint complications, reduces the amount of satellite data available for ocean color analysis.

In order to derive the water-leaving radiance, the contribution of Rayleigh and Mie aerosol scattering to the overall image data must first be known and considered as distinct variables. Corrections for Rayleigh scattering in the atmosphere have been developed by Gordon et al. (1988) and Gordon and Wang (1994).

Gordon et al. (1988) derived a method for accurately computing the Rayleigh scattering value as a function of the solar angle, the sensor viewing angle, the surface Fresnel reflectance, surface atmospheric pressure, surface wind speed, extraterrestrial solar irradiance, Rayleigh scattering optical thickness, and ozone optical thickness. Gordon and Wang (1994) and Gordon (1997) expanded upon the aforementioned Rayleigh scattering correction algorithm in the development of new atmospheric correction algorithms for the SeaWiFS and MODIS sensors,

respectively. The two new Rayleigh scattering corrections are applicable for the global ocean when the solar angle and the viewing angle of the sensor are known.

The impact of aerosol scattering, on the other hand, is more difficult to discern, especially in a high-sediment water body like Lake Pontchartrain. Aerosol correction cannot be accomplished through theoretical physical models, but rather it requires measurements made by the satellite sensors themselves across multiple wavelengths (Robinson 2004). Standard aerosol correction algorithms are often ineffective in coastal areas (Hu et al. 2000; Walker and Hammack 2000) so various techniques for aerosol correction have been developed specifically for coastal areas including Atchafalaya Bay (Walker and Hammack 2000), the Gulf of Maine (Hu et al. 2000), Tampa Bay (Hu et al. 2004), Mobile Bay (Zhao et al. 2011), Apalachicola Bay (Wang et al. 2010), and coastal areas of the Western Pacific near China (Wang et al. 2012), among others.

The most common method for aerosol correction in both coastal and deep ocean waters involves the use of the NIR channel. The "black pixel assumption," which builds upon the principle that water is a near-perfect absorber of light in the NIR wavelengths, states that the radiance value of the darkest pixel in an NIR image is representative of aerosol scattering alone (Siegel 2000). For Case 1 deep water, away from major sources of non-phytoplankton scattering and absorption, the radiance at NIR wavelengths is used to detect aerosol scattering. In Case 2 coastal and estuarine waters, however, aerosol correction is more problematic. Application of the standard Case 1 aerosol correction method to Case 2 waters yields imagery that is over-corrected for aerosols and therefore yields erroneous reflectance measurements. Thus, a simplified method of aerosol correction, called the "clear-water pixel method (CWP)," provides an acceptable way of estimating aerosols for Case 2 waters. The "CWP" method used in this research entails

identification of a pixel or group of pixels on the continental shelf or in deeper water where the water reflectance was minimal in the NIR channel. The reflectance of the "CWP" value was then subtracted from all Rayleigh-corrected reflectance values of the corresponding red band image. The CWP method was used for aerosol correction of all MODIS imagery during the 2016 BCS diversion event as discussed in Chapter 4.

There is a disadvantage with this method, however. The NIR aerosol correction method works under the assumption that the type and size of aerosol particles are uniform across the viewing area, which is unlikely to be the case in all instances. Therefore, it is important to choose a pixel value at a longitude nearest to the area of interest, but also at a sufficient distance off the coast. This approach ensures that the representative aerosols at the precise location of the CWP are as similar as possible to the study area while remaining uncontaminated by sediment or other constituents (Walker and Hammack 2000).

2.1.2 Remote Sensing of Suspended Sediment Concentration

Monitoring of suspended sediment concentration (SSC) is crucial to understanding the health of an estuary like the Lake Pontchartrain Basin. The SSC is a composite measurement of both inorganic sediment concentration (ISC) and organic suspended sediment concentration (OSC). The sediments in a water body have an impact on primary production, nutrient dynamics, and many other chemical and biological processes. For example, higher SSC values can either increase or decrease primary production, depending on water depth. Suspended sediments also have an effect on the movement of shorelines and changes in underwater bathymetry. Sediment concentrations measured in Lake Pontchartrain have been found to correlate with the amount of discharge of sediment-laden water from the Lake's tributaries and also with resuspension of sediments by wind waves due to the Lake's shallow depth (less than 4 m, on average) (Booth et

al. 2000; McCorquodale et al. 2009). As will be discussed in Chapter 3, the opening of the BCS in 2016 resulted in a marked increase in SSC and ISC values in Lake Pontchartrain.

Numerous studies have shown the effectiveness of satellite-borne sensors for monitoring SSC in coastal and estuarine environments (e.g., Stumpf and Goldschmidt. 1992; Walker 1996; Hu et al. 2000; Walker and Hammack 2000; Walker 2001; Myint and Walker 2002; Hu et al. 2004; Ramatchandirane et al. 2017). MODIS sensors in particular have been used successfully to map SSC in areas such as Mobile Bay (Zhao et al. 2011), Tampa Bay (Hu et al. 2004) and the northern Gulf of Mexico including Lake Pontchartrain (Miller and McKee 2004). Previous studies employed the use of AVHRR and the (now-defunct) SeaWiFS sensors for monitoring SSC in coastal environments similar to Lake Pontchartrain. However, neither AVHRR sensors nor SeaWiFS have a spatial resolution greater than 1 km, whereas MODIS sensors have a higher resolution of 250 m in the red and NIR bands. The MODIS sensors are, therefore, particularly useful for coastal research involving SSC because of their ability to perform more accurate aerosol correction using the NIR bands.

As discussed in Section 2.1, remote sensing reflectance is a measure of the ratio of backscatter to absorption. However, ISC and OSC affect reflectance in different ways so it is important to distinguish between these two variables when considering remote sensing in a coastal environment like Lake Pontchartrain. Measurement of SSC takes into account both the inorganic and organic sediment values. However, in the absence of in-water measurements, it is difficult to determine to what degree the absorption by organic material or backscattering by inorganic material influences the remote sensing reflectance when measuring the overall SSC.

Absorption by organic material can reduce reflectance in the red wavelengths considerably, even during periods of higher ISC (Myint and Walker 2002; Hu et al. 2004) which

can lead to inaccurate estimates of ISC. Therefore, it is necessary to isolate the ISC in order to get a more precise assessment of the overall sediment regime. Furthermore, particle size and mineral composition also play a role in reflectance. For example, finer-grained sediments, such as clay, with more particles, contribute to more scattering and, thus, higher reflectance. Therefore, an understanding of the local area sediment regime is also important for development of accurate algorithms for ISC of a local area. Water and sediment dynamics vary in different coastal systems and change over time, which also reinforces the need for local area algorithm development.

The critical factor in monitoring sediments through remote sensing is the use of the red band reflectance (MODIS Band 1: 620 – 670 nm) because ISC primarily backscatter light in the red wavelengths, especially when ISC values are high. When the effects of backscattering by ISC far exceed those of absorption by phytoplankton or organic material, such as what was observed during the 2016 BCS diversion event, the reflectance at the red band can be attributed primarily to the backscatter by ISC. When the red band reflectance is then compared to the *in-situ* ISC values through simple regression analysis, a predictive algorithm for ISC can be derived. This type of regression analysis technique has been used with success for remote sensing of SSC in coastal Louisiana (Walker and Hammack 2000; Myint and Walker 2002) because of the dominance of ISC backscatter in coastal Louisiana river plumes. The process of predictive algorithm development for ISC of the 2016 BCS diversion event is discussed in Chapter 5.

2.2 Importance of the Bonnet Carré Spillway to Lake Pontchartrain Ecology

2.2.1 Nutrient Dynamics

The construction of levees along the Mississippi River has converted much of what was once wetland or forest into farmland (Abernethy and Turner 1987). Turner and Rabalais (1991)

measured the changes in northern Gulf of Mexico water quality for the twentieth century that resulted from the increased use of fertilizers in the Mississippi River watershed; specifically, they studied the mean concentrations of nitrate, silicate, and phosphorus at various time intervals. Their study found that increased nitrogen and phosphorus fertilizer usage coincided with an increase in Mississippi River nitrogen and total phosphorus concentrations, but silicates in coastal waters decreased in concert with increased phosphorus fertilizer usage (Turner and Rabalais 1991). The decrease in silicon was hypothesized to be a result of increased diatom growth, which was stimulated by the increased phosphorus concentrations within the tributaries of the Mississippi River watershed (Turner and Rabalais, 1991).

The eutrophication of the Mississippi River is a contributing factor to the annual northern Gulf of Mexico phytoplankton blooms which lead to occurrences of hypoxic conditions (Rabalais et al. 1991; Turner and Rabalais 1991; Justic et al. 1993; Turner and Rabalais 1994; Burkart and James 1999; Walker and Rabalais 2006). Summertime Gulf of Mexico hypoxia events can extend over an area of 9,000 km^2 or greater and are often typified by large fish and intervertebrate kills (Turner and Rabalais 1994; Rabalais 2015). The decrease in Mississippi River water quality is also of concern for Lake Pontchartrain because of the high influx of Mississippi River water into the Lake that occurs during a BCS diversion event.

Day et al. (1999) found that the influx of Mississippi River water into Lake Pontchartrain simultaneously decreased salinity and increased nutrient levels during the 1997 BCS opening (17 March – 17 April), specifically along the southern portion of the Lake. Their study found that, at two southern Lake Pontchartrain measurement stations, nitrogen and total phosphorus levels remained high for a month after the spillway's closure and then rapidly returned to pre-opening levels by mid-June 1997 (Day et al. 1999). Lake Pontchartrain salinity levels, however, showed a

more gradual increase: at one southern station, salinity did not return to pre-opening levels until late August 1997 (Day et al. 1999). Roy et al. (2013) noted that discharge from northern Lake Pontchartrain tributaries was significantly higher than usual in the months during and after the 1997 BCS event, which could have played a role in the lag in salinity rebound.

During the 2008 BCS opening, Mize and Demcheck (2009) obtained continuous (hourly) nitrate concentrations at a station in the south-central area of Lake Pontchartrain and determined that nitrates peaked with the initial arrival of the Mississippi River water to the sampling location. A steady collapse in nitrate levels was observed thereafter, with a return to pre-diversion nitrate levels within two weeks of the closing of the BCS. Discrete sampling of chlorophyll *a* and phytoplankton taxa from 8 April to 3 October showed a marked phytoplankton community response to the Mississippi River water input. The phytoplankton community composition changes were not attributed to normal seasonal activity, but rather to a direct response to the changes in Lake Pontchartrain water quality (Mize and Demcheck 2009). Bargu et al. (2011) also observed a similar change in overall phytoplankton community shifts, including a harmful cyanobacteria algal bloom that was observed as the nutrient levels decreased. It could not be concluded whether the harmful algal bloom was a direct result of the BCS diversion or natural shifts in other local environmental conditions. White et al. (2009) hypothesized that the diversion of large amounts of inorganic nitrogen via the BCS (up to 7.6% of the total Mississippi River dissolved nitrogen load) may have helped to reduce the overall Gulf of Mexico hypoxia zone in the summer of 2008.

Through comparisons of the 1997, 2008, and 2011 BCS diversion events, Roy et al. (2013) found that the high nutrient influx in each of the BCS diversion events correlated with higher chlorophyll *a* concentrations, but they did not find that one particular phytoplankton

species dominated. For example, in contrast to both the 1997 and 2008 events, their study found that cyanobacteria harmful algal blooms were negatively impacted by the influx of Mississippi River water during the 2011 BCS diversion event, likely due to the high turbulence of water present during that event compared to previous diversions and the timing of the event (Roy et al. 2013).

CHAPTER 3: DATA SOURCES AND SOFTWARE

3.1 Lake Pontchartrain Data Collection and Lab Analyses

Data for developing a sediment algorithm were collected on several dates from January to March in 2016, during and after the opening of the BCS. More specifically, surface suspended sediment suspended data from Dr. John White of Louisiana State University's Department of Oceanography and Coastal Sciences (LSU DOCS) were collected on 15, 24, and 29 January; 5, 19, and 26 February; and 25 March 2016. Dr. White's data is hereafter referred to as Dataset 1.

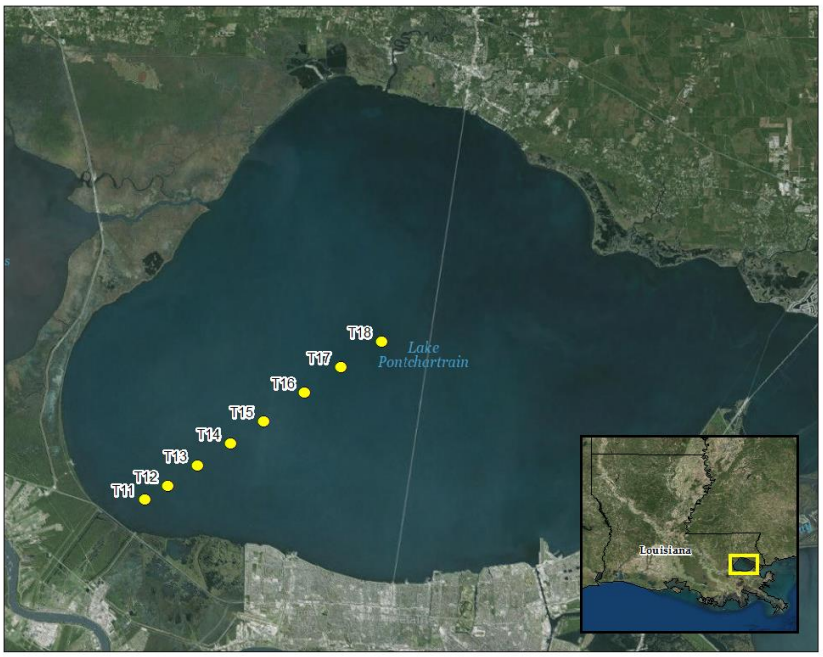

Figure 3.1: Dataset 1 station locations in Lake Pontchartrain

Data were also collected by Dr. Nan Walker of LSU DOCS on 23 January and 13 March 2016. Dr. Walker's data is hereafter referred to as Dataset 2. The locations of Dataset 1 used in this study have each been assigned a specific station identifier ranging from T-11 to T-18 (Figure 3.1), while those from Dataset 2 are delineated by numbers (Figures 3.2 and 3.3, respectively). Data for stations T11-T12 and T17-18 on 15 January were discarded due to cloud contamination in the satellite imagery. Data from T14 for 19 February and from T18 for 26 February could not

be used for this project. Surface water samples were collected 5-10 cm below the water surface so as to avoid surface film contamination of water samples.

Figure 3.2: Dataset 2 23 January 2016 station locations in Lake Pontchartrain

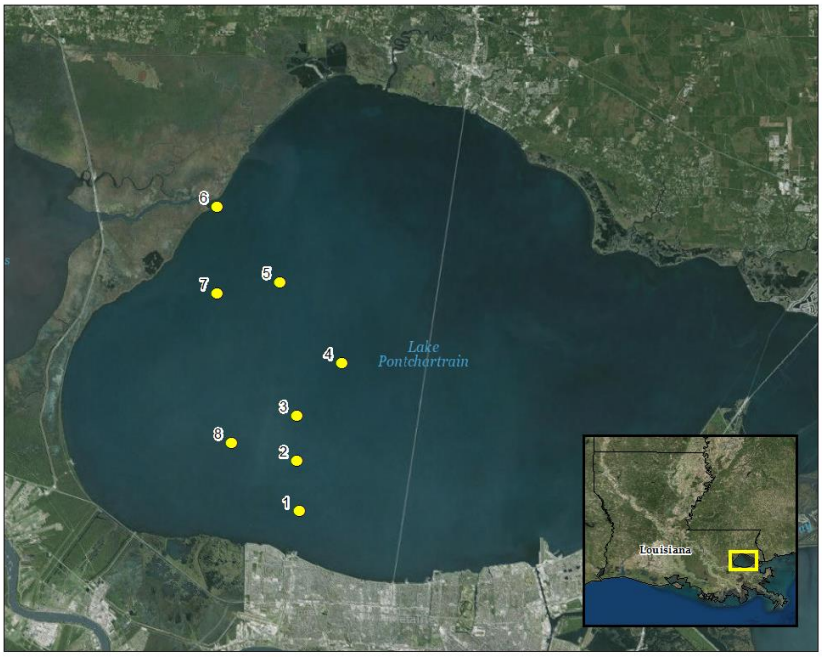

Figure 3.3: Dataset 2 13 March 2016 station locations in Lake Pontchartrain

Field-collected data from 23 January and 13 March were analyzed by the LSU Wetland Biogeochemistry Analytical Services (WBAS) to determine SSC, OSC, and ISC. Water samples from Dataset 1 were analyzed by the LSU Wetland and Aquatic Biogeochemistry Lab (WABL) and by Robert Iles. Both laboratories followed the methods of the American Public Health Association to determine the three sediment concentration measures (APHA 2005). Multiple water samples were collected at each station on 23 January and 13 March. No sediment data were collected at station 6 on 13 March.

In-situ above-water remote-sensing reflectance data (R_{rs} (λ)) were collected for wavelengths ranging from 290 nm to 1096 nm at each of the 13 March stations using a GER 1500 spectroradiometer using the methods of Lee et al. (1997), Mobley (1999), and Hu et al. (2004). At each station, three separate measurements were taken: upward radiance from the water surface (L_u) measured 30° from nadir, downwelling sky radiance (L_{sky}) measured 30° from overhead, and radiance off of a horizontally held standard Spectralon reflectance plaque (L_{card}) (Hu et al. 2004). R_{rs} (λ) was calculated using the following equation where 'ρ_{card}' is the manufacturer-provided plaque reflectance and 'ρ_f' is Fresnel reflectance (~0.028) (Mobley 1999; Hu et al. 2004):

$$R_{rs} = \rho_{card} (L_u - \rho_f L_{sky})/(\pi L_{card})$$

The resulting R_{rs} (λ) values were then multiplied by π in order to derive reflectance R (in %).

3.2 *In-situ* Barataria Bay Collection

An additional 11 samples of sediment data were collected on 5 April along a transect from Barataria Bay to the coastal ocean by the Water Institute of the Gulf and subsequently processed by WBAS to determine SSC. Barataria Bay measurements were used in the Lake Pontchartrain algorithm development to increase data points with low sediment concentrations.

Since this field region should contain similar sediment constituents to the Lake Pontchartrain Basin, these SSC data were considered usable for ISC algorithm development at least at low sediment levels, which were important to extend the algorithm into the lower concentration range values.

3.3 NASA MODIS Aqua/Terra Imagery

Daily imagery from the NASA Earth Observing System (EOS) satellites Aqua (EOS PM-1) and Terra (EOS AM-1) is collected and distributed by the NASA Ocean Biology Processing Group (OBPG). The Aqua satellite orbits the Earth from south to north (ascending) during the day, while the Terra satellite orbits north to south (descending) during the day. The satellites are designed to cover the same area about three hours apart. This difference in orbit and temporal coverage necessitated the use of data from one or the other satellite, depending on the date and atmospheric conditions at the time of data collection.

All satellite images used in this project were initially collected as Level 1A imagery (OBPG 2014) in March 2016 from OBPG at https://oceancolor.gsfc.nasa.gov/cgi/browse.pl?sen=am. The acquired Level 1A images were processed first to Level 1B imagery using a script developed by Alaric Haag at the LSU Earth Scan Laboratory. The Level 1B images were then processed to Level 2 imagery using the OBPG's SeaDAS software. The output Level 2 reflectance images were used for sediment algorithm development. Data captured by the Terra satellite were used for 15 January and 24 and 25 March. All other dates (23 and 29 January; 5, 19, and 26 February; and 13 March) used data from the Aqua satellite.

3.4 Lake Pontchartrain Tributary Discharge

Water discharge data from the USGS NWIS from various Lake Pontchartrain tributaries were collected to reveal how sediment plume dispersal and concentration were impacted by freshwater stream discharge from non-BCS sources. Specifically, discharge rates of varying intervals for the period from 1 January to 31 March 2016 were collected for every half-hour for the Amite River near Denham Springs (USGS Station 7378500) and Tangipahoa River at Robert (USGS Station 7375500), and every 15 minutes for the Tchefuncte River near Folsom (USGS Station 7375000), Tickfaw River at Holden (USGS Station 7376000), and Natalbany River at Baptist (USGS Station 7376500). Additionally, half-hour discharge rates were collected from the Pearl River near Bogalusa (USGS Station 02489500) to provide insight into the plume's movement as portions of the plume exited Lake Pontchartrain.

3.5 Water Elevation Data

Daily water level elevation data were collected for the following gages: Chef Menteur near Lake Borgne (USACE #85750), the Rigolets near Lake Pontchartrain (USACE #85700), and the Mississippi Sound at Grand Pass (USGS #300722089150100).

3.6 Surface Meteorological and Oceanographic Data

Data of temperature, wind direction, wind speed, and atmospheric pressure were collected from http://www.ndbc.noaa.gov for two National Data Buoy Center (NDBC) stations within the Lake Pontchartrain Basin: Frenier Landing (FREL1) and New Canal Station (NWCL1). The NDBC station locations are shown in Figure 3.4. Additional wind data from the Louis Armstrong New Orleans International Airport (MSY) were collected from the National Climatic Data Center quality controlled Local Climatological Data site at https://www.ncdc.noaa.gov/qclcd/QCLCD.

Figure 3.4: NDBC station locations in Lake Pontchartrain

3.7 Software Used

The NASA OBPG's SeaDAS software (version 7.4) was used to process imagery from Level 1B to Level 2 using the software's l2gen script. Additional mapping was done in ESRI ArcMap (version 10.5).

CHAPTER 4: AEROSOL CORRECTION FOR THE 2016 BONNET CARRÉ SPILLWAY DIVERSION

Chapter 3 presented the data collected for all chapters of the overall project. Chapter 4 explores the effectiveness of the clear-water pixel (CWP) method as a means of aerosol correction in Lake Pontchartrain during the 2016 BCS diversion. Aerosol correction is a critical step in the processing of coastal and ocean remote sensing imagery, but traditional algorithms did not perform well in Lake Pontchartrain due to the high reflectance values caused by the influx of Mississippi River water and the sediment it contained. Therefore, the development of an aerosol correction method specific to Lake Pontchartrain was necessary. This chapter presents the method for aerosol correction of the red channel (645 nm) of the MODIS imagery.

4.1 Methods

4.1.1 The Clear Water Pixel Method

The black pixel assumption states that the water-leaving radiance value for clear water (i.e. water with few or no particulates) is 0 in the near-infrared (NIR) portion of the spectrum because of the high absorption coefficient of water in the NIR (Siegel 2000). Aerosol correction models can be inaccurate in sediment-laden waters like Lake Pontchartrain because they use NIR channels to correct for aerosol interference. While these algorithms are useful for Case 1 waters dominated by chlorophyll absorption, Case 2 waters, such as Lake Pontchartrain, are typified by high backscattering from sediments, absorption by CDOM, and absorption by organic sediments such as marsh material. Additionally, cloud masking techniques, which identify high reflectance and temperature gradients as clouds, often mistakenly evaluate high sediment waters as clouds in the masking process. As much as 90% of the signal measured by ocean color sensors can be attributed to atmospheric influence (Siegel 2000), but traditional NASA algorithms generally overcorrect for aerosols and clouds in Case 2 waters and consequently discard useful data.

The CWP method employs the use of Rayleigh-corrected imagery before application of an aerosol correction. The purpose of the CWP method is to provide an estimate of aerosol scattering to be applied across the region of interest. This is accomplished by selecting a pixel in the open ocean or on the continental shelf which has the lowest reflectance (i.e., a 'CWP') in the NIR channel (859 nm). Because the reflectance of clear water is assumed to be 0 at this wavelength, the reflectance value of the darkest pixel in a non-aerosol corrected image is assumed to be due to the contribution of aerosols alone (Robinson 2004). The CWP pixel is not necessarily the same value or at the same location for each date because of the varying oceanic and atmospheric conditions between dates. When using the CWP method for Lake Pontchartrain images, only areas of the northern Gulf of Mexico due south of Lake Pontchartrain (approximately between longitude 90.5º W and 89.5º W) and within ~100 km of the coast were used to find an acceptable CWP so that similar atmospheric conditions as were present above Lake Pontchartrain could be assumed. Table 4.1 contains the CWP value for each image for each date in 2016 for which *in-situ* data was available (see Appendix B for additional data).

Table 4.1: Clear-water pixel value (%/100) from the MODIS near-infrared band (859 nm) for each image date for which water samples were available in 2016

Date	CWP value
15-Jan	0.0058
23-Jan	0.0023
24-Jan	0.0029
29-Jan	0.0049
5-Feb	0.0048
19-Feb	0.0080
26-Feb	0.0100
13-Mar	0.0090
25-Mar	0.0074

The reflectance value (in %/100) of that pixel was then subtracted from the reflectance value of each pixel in the red channel (645 nm) on dates for which field-collected data were

available. The resulting difference is the Rayleigh and aerosol-corrected reflectance for the red channel, hereafter referred to simply as “atmospherically-corrected reflectance”.

4.1.2 Field Spectroradiometer Data

The 13 March 2016 field trip was taken to collect spectroradiometer reflectance data to test the accuracy of the CWP method for this lake. At each station, spectroradiometer water-leaving radiance (L_w) data were collected at the stations shown in Fig.3.3. The equation described in Section 3.3 was applied to the spectrometer radiance measurements to compute remote sensing reflectance, which was multiplied by pi to estimate reflectance in (in %). The radiometer measurements were then compared to the satellite-derived atmospherically-corrected reflectance (%) values for each of the eight stations.

4.2 Results

Figure 4.1 shows three different satellite images for 13 March 2016. The concepts of scattering and absorption are clearly illustrated in images (a) and (b), which depict the original non-aerosol corrected reflectance imagery. Lake Pontchartrain appears darker in image (b), which is the NIR reflectance, because of how greatly water absorbs light at that wavelength. Image (a), the red channel reflectance, appears almost uniformly bright because of the high scattering due to ISC at that wavelength. Image (c) is the resulting image after the CWP aerosol correction technique was performed and depicts the atmospherically-corrected reflectance of the red channel. The Lake still appears bright in image (c), but the plumes of sediment are easier to distinguish from areas of less turbid water. Although some clouds are present in the 13 March imagery, no field stations were near enough to the cloud-affected pixels to have been contaminated. Additionally, wind data from NOAA Lake Pontchartrain stations FREL1 and NWCL1 indicate that wind speeds averaged less than 3 m s^{-1} during data collection for 13

March, which gives added confidence in the accuracy of the field-collected data (Hu et al. 2004). The ranges of reflectance were adjusted differently for each of the images in Figure 4.1, which is why (c) appears brighter than (a).

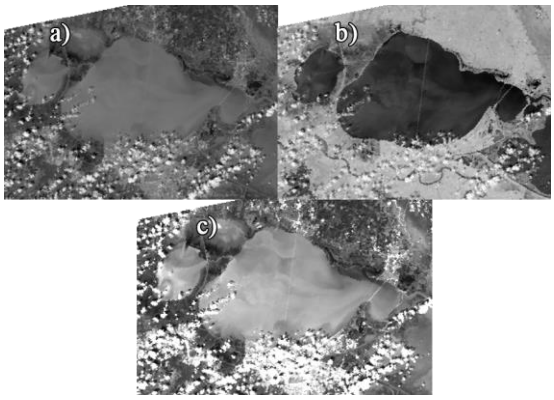

Figure 4.1: 13 March 2016 imagery: a) MODIS Rayleigh-corrected red band reflectance (645 nm); b) MODIS Rayleigh-corrected near-infrared band reflectance (859 nm); c) Atmospherically-corrected red band reflectance

The field-collected spectroradiometer reflectance values did not differ significantly from the atmospherically-corrected MODIS imagery, as confirmed by the low RMSE value of 0.004. Figure 4.2 shows the spectroradiometer reflectance values plotted against the atmospherically-corrected reflectance percent values.

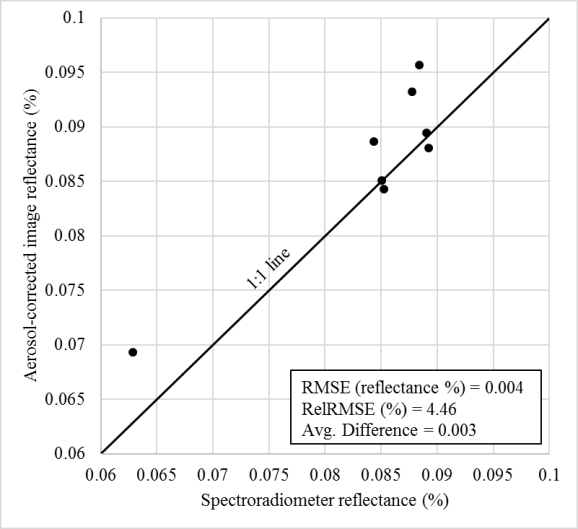

Figure 4.2: Field spectroradiometer reflectance values (%/100) compared to satellite atmospherically-corrected image reflectance values (%/100) for 13 March 2016.

CHAPTER 5: DEVELOPMENT OF A PREDICTIVE INORGANIC SEDIMENT ALGORITHM FOR LAKE PONTCHARTRAIN SUSPENDED SEDIMENTS

5.1 Methods

5.1.1 Derivation of Sediment Concentration

Half-liter water samples were obtained from Lake Pontchartrain on 23 January and 13 March and filtered in the WBAS with a filter size of 0.7 microns to determine SSC. One-liter water samples were obtained from Lake Pontchartrain on 15, 24, and 29 January; 5, 19, and 26 February; and 25 March and filtered in the LSU WABL to determine SSC. The resulting filtered, dried, and weighed samples were then ashed in a muffle furnace (Cole-Parmer Stabletemp Furnace) at 550°C overnight (~4 hours). The samples used were from eight stations T11-T18 (see Figure 3.1 for locations). Additionally, each sample was given a unique identifier ranging from 1 – 74.

Because the ashing process was conducted overnight, each set of samples had usually cooled to about 25°C by the morning. After removal from the furnace, the samples were then placed in a drying oven for 30 minutes in order to raise their temperature to ~70°C. After removal from the drying oven, the samples were placed in a dessicator and covered for 15 minutes to ensure that no lingering water was present in or on the samples (Figure 5.1).

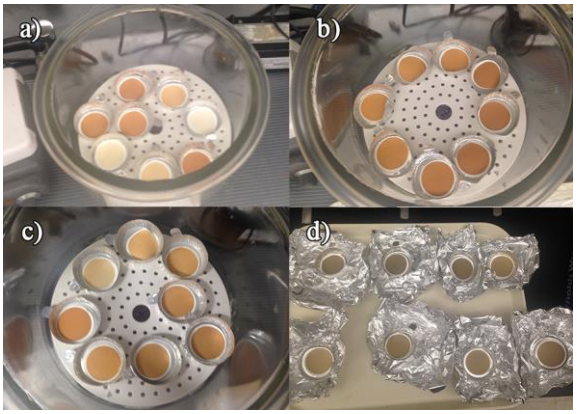

Figure 5.1: a) 15 January samples in dessicator post-ashing, b) 24 January samples in dessicator, c) 29 January samples in dessicator, d) 5 February samples pre-ashing

After removal from the dessicator, each sample was weighed individually to determine mass loss on ignition (LOI). The weight of the remaining material was the ISC. The difference between the pre-LOI sample weight (i.e., SSC) and ISC is the OSC.

5.1.2 Regression-based Sediment Algorithm Development

Regression analysis of the atmospherically-corrected reflectance values and the *in-situ* ISC values was performed in order to find a best-fit line whose equation could be used as a quantitative sediment algorithm for describing and predicting ISC. Data from the March field exercise were excluded from the algorithm development portion of the study due to an unusual precipitation event from 8–11 March 2016 which introduced copious amounts of river water and sediments from the Tchefuncte and Tangipahoa Rivers into Lake Pontchartrain. The newly introduced water masses may have differed from the inorganic sediment-rich Mississippi River water introduced by the BCS in the weeks prior and thus was eliminated from consideration for development of the Mississippi River sediment algorithm.

In order to obtain the best regression model, attempts were made to filter out less reliable data. Ideally, higher surface suspended sediment loads would produce a higher atmospherically-corrected reflectance percent (Wang et al. 2012), but that was not the case for all data. The data were analyzed separately for each date in order to single out any problematic dates or diagnose a particular variable that could reduce model accuracy. Specifically, a set of dates was selected that contained ISC quantities that would cover the entire range of reflectance values from low to high concentrations but which also contained fewer outliers than other dates. Furthermore, field samples not collected within 30 minutes of a satellite overpass were also discarded (Miller and McKee 2004). Various non-linear algorithms were investigated. In the final analysis, an exponential function was used to produce the sediment algorithm equation.

5.1.3 Application of Sediment Model

Aerosol correction of the acquired Rayleigh-corrected imagery was performed in accordance with the methods discussed in Chapter 4. The ISC algorithm equation was then applied to the resultant atmospherically-corrected imagery to estimate ISC for the entirety of Lake Pontchartrain. In the SeaDAS software, the "Band Math" tool was used to apply the equation to the atmospherically-corrected imagery for each date separately. This process solves the exponential model equation by substituting the reflectance value of each pixel of the imagery for the 'x' value of the function. The resulting value is the sediment concentration in mg L^{-1}.

5.2 Results

5.2.1 Sediment Concentration Values for the 2016 Bonnet Carré Spillway Event

Figure 5.2 shows the vast disparity between ISC and OSC for the 2016 BCS event. On only 5 occasions (out of the 74 total data points) was OSC greater than ISC (see Appendix A). Of those 5, only 1 data point was within the visible Mississippi River sediment plume. The other 4 instances were data points collected at the northeasternmost stations of Dataset 1 (T17 and T18) on days for which those stations were outside of the Mississippi River sediment plume.

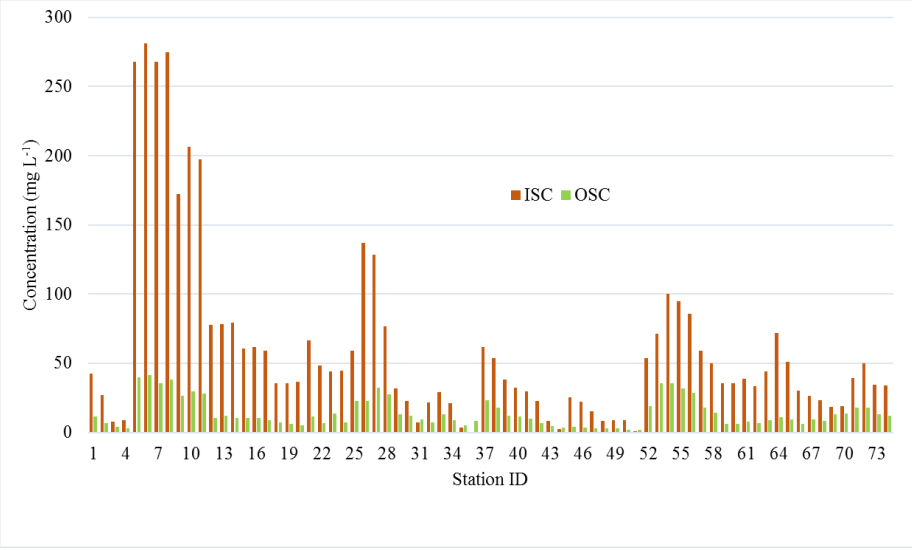

Figure 5.2: Inorganic (in brown) and organic (in green) sediment concentrations (mg L^{-1})

ISC constituted the dominant percentage of the overall SSC for most of the study period (Figure 5.3). As noted in Chapter 2, a higher concentration of organic material could possibly contaminate SSC reflectance, because it would be difficult to discern to what degree the inorganic material was scattering light in the red wavelengths while the organic material was absorbing light. However, the amount of organic material absorbing light was calculated to be small enough to ensure that the observed remote sensing reflectance for the study period could be attributed primarily to scattering by inorganic material. The additional steps taken to ash and subsequently weigh the sediment samples to calculate ISC were a potential source of error, but were considered small.

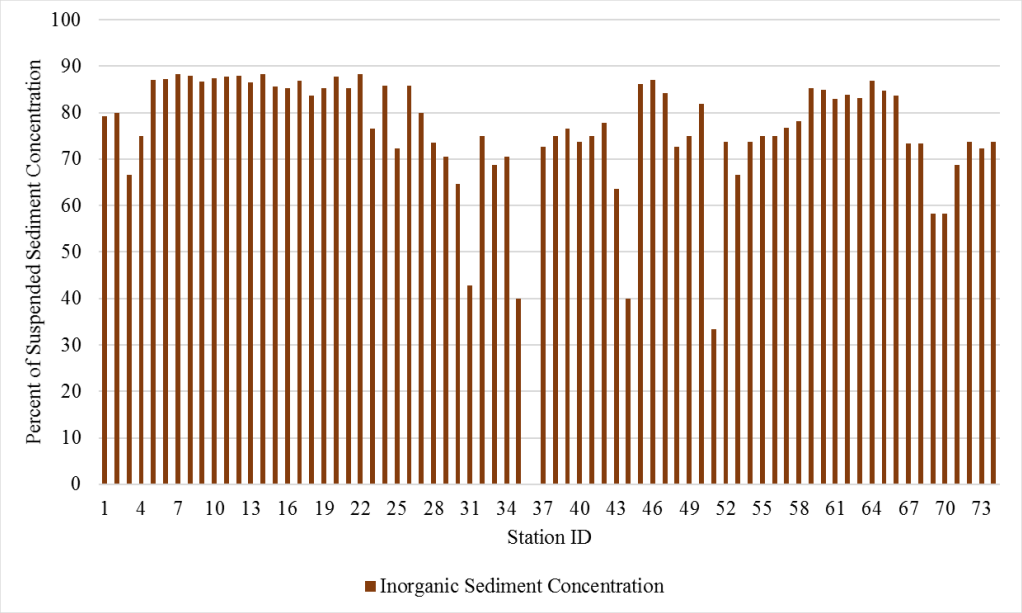

Figure 5.3: *In-situ* inorganic sediment concentration as a percentage of total suspended sediment concentration

5.2.2 New Lake Pontchartrain Sediment Algorithm

Regression models were derived using all available non-sunglint atmospherically-corrected imagery in tandem with *in-situ* data for each separate date individually with mixed results. Although some of the daily regression models exhibited higher r-squared values, none of

the regression analyses from the individual dates produced an optimized trendline function that could accurately predict values across the entire range of sediment concentrations. The 23 January data had the highest r-squared value, 0.9538 (n = 16), but lacked any data with an atmospherically-corrected reflectance less than 0.07 percent. The equation for that date was, therefore, inadequate since it lacked any data points in the lower reflectance range.

After adjusting for outliers as discussed in Section 5.1.2, the resulting data points spanned the entire range of atmospherically-corrected reflectance percentage values using data with fewer outliers. The dates used for this final calculation were 23 January, 26 February, and the 5 April Barataria Bay-shelf data. Figure 5.4 shows the exponential function produced as a result of the regression of the atmospherically-corrected imagery and the *in-situ* ISC data.

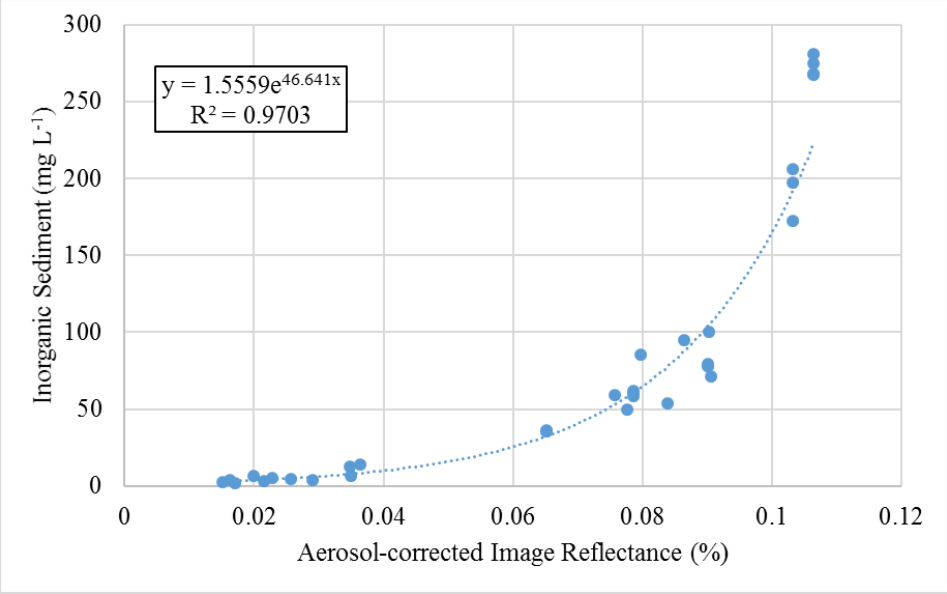

Figure 5.4: Inorganic sediment concentration (mg L^{-1}) and atmospherically-corrected MODIS image reflectance (%/100) for 23 January, 26 February, and 5 April

The ISC regression produced an r-squared of 0.9703 and optimal trendline shape representative of an ideal relationship between atmospherically-corrected reflectance and sediment concentration; i.e., reflectance increased with increased ISC, which is expected given

that reflectance would increase with the increased backscattering of light by the inorganic material. It is important to note that the low number of data points (n = 34) were a potential source of error.

The regression-derived ISC model equation for the 2016 BCS event in the Lake Pontchartrain Basin is

$$y = 1.5559e^{46.641x}$$

5.2.3 Model-Derived Sediment Concentration

Using the ISC regression algorithms, sediment concentrations (mg L^{-1}) were estimated and mapped for each of the dates of the study period. Figures 5.6 and 5.7 are the derived ISC maps for 23 January and 26 February, respectively. In the 23 January images, the highest sediment concentration of the sediment plume is clearly visible in the central portion of Lake Pontchartrain. The centralized plume has disappeared in the 26 February image, which is not surprising given that the BCS had been closed for over three weeks at that point. The lingering sediment in the 26 February images was likely resuspended from the Lake's floor by wind.

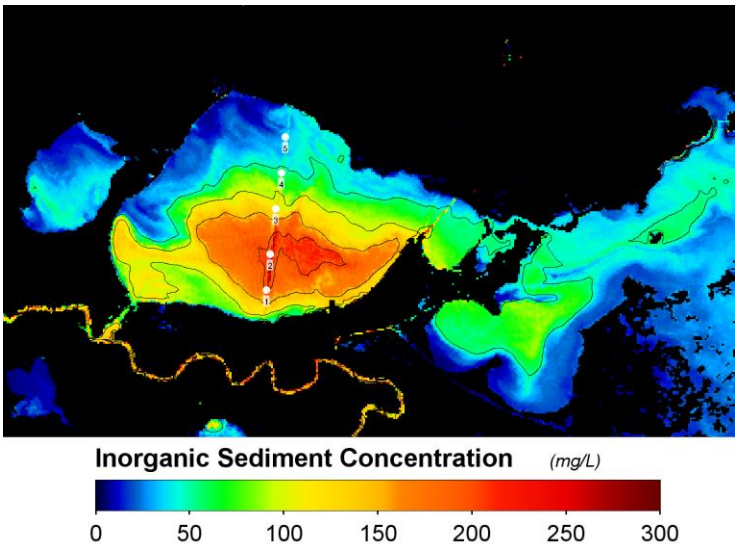

Figure 5.5: Model-derived inorganic sediment concentration (mg L^{-1}) for Lake Pontchartrain on 23 January 2016. Contour lines separate areas of differing concentration every 50 mg L^{-1} from 0 mg L^{-1} (blue) to 300 mg L^{-1} (dark red).

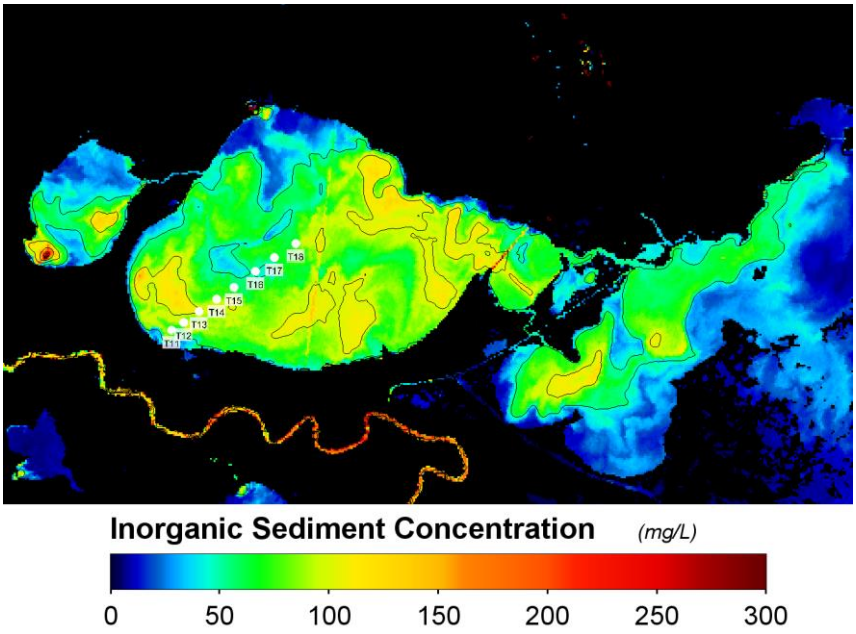

Figure 5.6: Model-derived inorganic sediment concentration (mg L^{-1}) for Lake Pontchartrain on 26 February 2016. Contour lines separate areas of differing ISC every 50 mg L^{-1} from 0 mg L^{-1} (blue) to 300 mg L^{-1} (dark red).

5.2.4 Algorithm Validation

Statistical analysis was performed on the model-derived ISC values (see Appendix C) by examining the root mean square error (RMSE) and relative RMSE (%) for the estimated ISC. RMSE was calculated using the expression

$$\text{RMSE (mg L}^{-1}) = \sqrt{\frac{\sum_{i=1}^{n} (y_i - SC_i)^2}{n}}$$

where y_i is the model-derived sediment concentration and SC_i is the field-derived sediment concentration for the same sample location. Relative RMSE was found using the expression

$$\text{Relative RMSE (\%)} = \left[\frac{\text{RMSE}}{SC_{max} - SC_{min}}\right] \times 100$$

where SC_{max} represents the maximum observed *in-situ* sediment value and SC_{min} the minimum observed *in-situ* sediment value. Figure 5.7 implies an acceptable ISC model performance as indicated by the RMSE value of 25.77 mg L^{-1}.

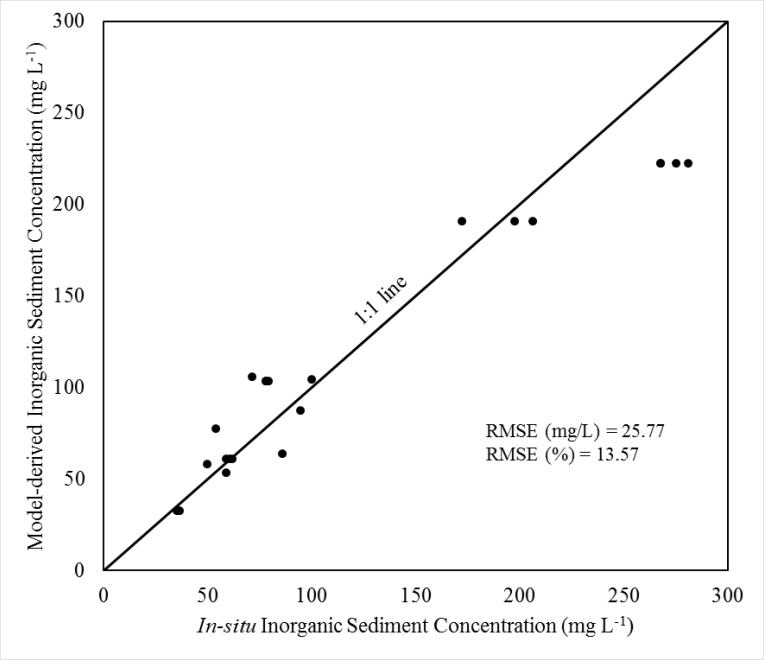

Figure 5.7: Inorganic sediment model verification for 23 January and 26 February data

CHAPTER 6: LAKE PONTCHARTRAIN SEDIMENT PLUME CHARACTERIZATION USING MODIS IMAGERY

In Chapter 5 the creation of a new ISC sediment model for the 2016 BCS diversion event was discussed. The ISC model was used to create images of sediment concentration for a range of dates in early 2016 during which the BCS was open as well as in the weeks after its closing.

In a five year study of the Mississippi River plume in the northern Gulf of Mexico, Walker (1996), using satellite imagery, identified river discharge and wind forcing as the primary mechanisms influencing plume variability. Of those two processes, the study noted that daily and shorter time-scale sediment plume changes were more attributable to wind forcing (Walker 1996). Chapter 6 examines the morphology and mean concentration of the Mississippi River plume in Lake Pontchartrain as a possible function of daily wind and BCS discharge rates before and during the BCS opening and after its closing. Sediment concentration images were created and, when coupled with wind speed, wind direction, water level, and Lake Pontchartrain tributary discharge observations, used to describe the Mississippi River sediment plume for the 2016 BCS diversion event.

6.1 Methods

New sediment concentration images were created using NASA SeaDAS software. Graded contours at 50 mg L^{-1} concentration increments were added to each MODIS image to distinguish more easily the areas of differing sediment concentration. The software offers the capability of providing statistical data about a region-of-interest. Three separate regions-of-interest were analyzed for the imagery: 1) Lake Pontchartrain as a whole, 2) the pixels contained within the 50 mg L^{-1} isopleth, and 3) the pixels within the 100 mg L^{-1} isopleth. Because the suspended sediment was so fragmented and distributed throughout the Lake in the 8 to 27 February images, the mean sediment concentration was calculated only for the Lake

Pontchartrain region-of-interest for those dates. Pixels affected by the reflectance of three Lake Pontchartrain bridges were discarded from all analyses: the Lake Pontchartrain Causeway, a north south bridge bisecting the Lake, as well as the Highway 11 and Twin Span bridges. Additionally, pixels within 1 km of land were discarded so as to avoid being contaminated by errant land-reflected light.

6.2 Results

Tables 6.1 and 6.2 present the results of the sediment plume quantification using the new MODIS ISC model. For the dates 11 January to 7 February, observations of mean, minimum, and maximum inorganic sediment concentration are presented for the 50 mg L^{-1} (Table 6.1) and 100 mg L^{-1} isopleths (Table 6.2), respectively, as well as the area in km^2 of the two plume concentration isopleths. For the full range of dates 11 January to 27 February, observations of mean, minimum, and maximum sediment concentration were calculated for the entirety of Lake Pontchartrain minus pixels near land or containing bridges, as noted in Section 6.1 (see Appendix D). Although values of mean Lake Pontchartrain ISC were calculated and are briefly discussed in this Chapter, the sediment model did not account for any potential absorbing material (e.g. CDOM or chlorophyll *a*) present in water outside of the Mississippi River sediment plume; therefore, the sediment model is most valid for those areas of higher sediment concentration within the visible Mississippi River sediment plume where ISC was known to be greater than OSC (Figure 5.2). Additionally, the sediment model was developed using MODIS Aqua imagery and is not necessarily considered valid for Terra imagery. However, some Terra images were still useful for describing the overall plume morphology. Data from Terra imagery is distinguished from that of the Aqua imagery in the data tables with an asterisk on the date value of the Terra images.

Table 6.1: 50 mg L^{-1} inorganic sediment plume statistics for 11 January to 7 February. MODIS Terra images indicated with asterisk next to date. Otherwise, MODIS Aqua images used for remaining dates.

Date	Plume Area (km^2)	% of Lake Area	Mean (mg L^{-1})	Max (mg L^{-1})	Min (mg L^{-1})
11-Jan	178.63	10.91	70	141	27
13-Jan	156.68	9.57	167	333	22
16-Jan	265.79	16.24	108	172	14
17-Jan*	320.15	19.56	79	123	40
18-Jan	535.56	32.72	146	294	17
19-Jan*	587.22	35.87	128	239	33
23-Jan	1116.91	68.23	123	234	38
24-Jan*	1041.64	63.63	149	296	29
28-Jan	1057.28	64.59	150	295	11
29-Jan	1053.75	64.37	171	282	20
5-Feb	1081.55	66.07	114	234	35
7-Feb	903.84	55.21	116	287	38

Table 6.2: 100 mg L^{-1} inorganic sediment plume statistics for 11 January to 7 February. MODIS Terra images indicated with asterisk next to date. Otherwise, MODIS Aqua images used for remaining dates.

Date	Plume Area (km^2)	% of Lake Area	Mean (mg L^{-1})	Max (mg L^{-1})	Min (mg L^{-1})
11-Jan	15.65	0.96	111	141	79
13-Jan	110.59	6.76	202	333	53
16-Jan	130.79	7.99	134	172	62
17-Jan*	49.20	3.01	106	123	93
18-Jan	393.83	24.06	171	294	68
19-Jan*	419.71	25.64	147	239	61
23-Jan	683.58	41.76	150	234	89
24-Jan*	812.25	49.62	169	296	71
28-Jan	894.40	54.64	165	295	77
29-Jan	905.94	55.34	184	282	79
5-Feb	535.95	32.74	147	234	62
7-Feb	460.97	28.16	159	287	90

6.2.1 Relationships between Bonnet Carré Spillway Discharge and Sediment Plume Areal Variability

The BCS was open for 22 days from 10 to 31 January. The number of Spillway bays open was increased each day, thereby increasing the daily discharge rate, from 10 until 19 January, after which time the daily discharge rate plateaued between 5,000 and 6,000 $m^3 s^{-1}$. From 25 to 31 January, Spillway bays were closed each day, with daily discharge rate decreasing and ultimately ceasing by 1 February.

Figure 6.1 compares the daily BCS discharge rate to the spatial area of the 50 mg L^{-1} ISC plume isopleth. The plume area appeared to increase in concert with the daily Spillway discharge rate, with an approximate three day lag. As discharge rate plateaued, the plume's area followed suit, itself plateauing just above 1,000 km^2 and remaining near peak level even after BCS discharge was reduced. The overall plume area did not begin to decrease until at least six days after the Spillway was closed. These observations would seem to indicate that the plume's total area was regulated by the daily Spillway discharge rate while the Spillway was open and within the week after its closure.

The 100 mg L^{-1} ISC plume isopleth's spatial distribution also appeared linked to the BCS daily discharge rate, although it did not achieve the same areal size as the 50 mg L^{-1} isopleth (Figure 6.2). While there was a trending increase in the 100 mg L^{-1} ISC plume area with daily discharge rate increase, a slightly increased lag was observed as compared to the 50 mg L^{-1} ISC plume area. The higher concentration plume area collapsed more quickly after the Spillway closure. While the 50 mg L^{-1} ISC plume area remained at its peak for nearly a week after the Spillway closure, the 100 mg L^{-1} isopleth area was reduced by 40% within five days of closure.

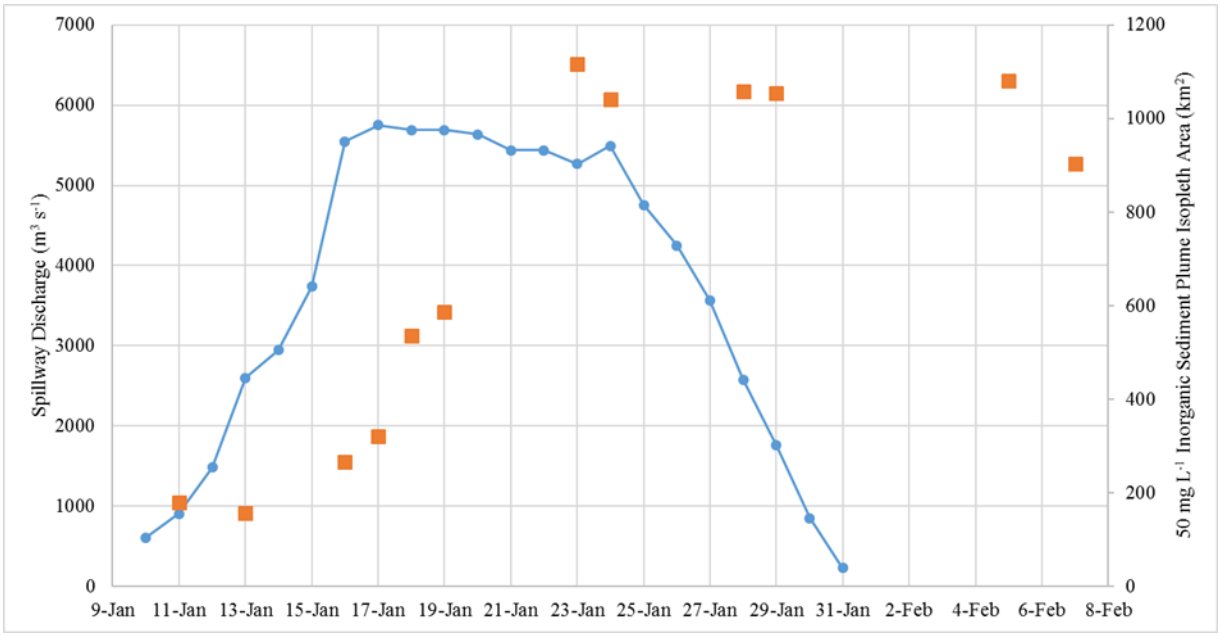

Figure 6.1: Bonnet Carré Spillway daily discharge rate (m^3 s^{-1}) (blue circles connected by lines); 50 mg L^{-1} plume area (km^2) (orange squares).

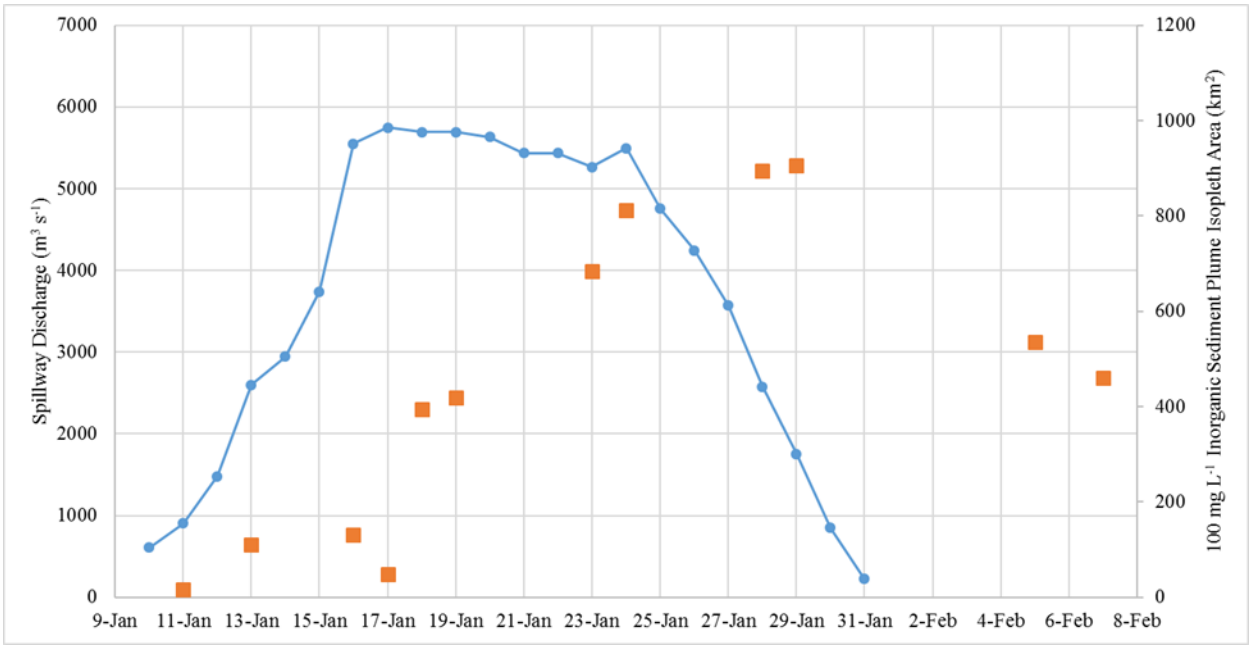

Figure 6.2: Bonnet Carré Spillway daily discharge rate (m^3 s^{-1}) (blue circles connected by lines); 100 mg L^{-1} plume area (km^2) (orange squares).

At its greatest areal distribution for the timeframe of 11 January to 7 February, the 50 mg L^{-1} ISC plume was distributed over approximately 68% of the total area of Lake Pontchartrain;

the 100 mg L^{-1} ISC plume maximum areal distribution covered approximately 55% of total Lake area for the same timeframe.

6.2.2 Observations of Plume Motion and Areal Change

Figure 6.3 displays the first four cloud-free images after the BCS opening: 11, 13, 16, and 17 January. These images span the first week of the diversion event. The eastward-leading edge of the 50 mg L^{-1} isopleth was found to be 23 km from the BCS on 11 January, the day after the Spillway opening. However, some leakage from the Spillway occurred in the days before the BCS opening, so the plume size for that date may not necessarily be attributable to discharge into the Lake after the Spillway opening.

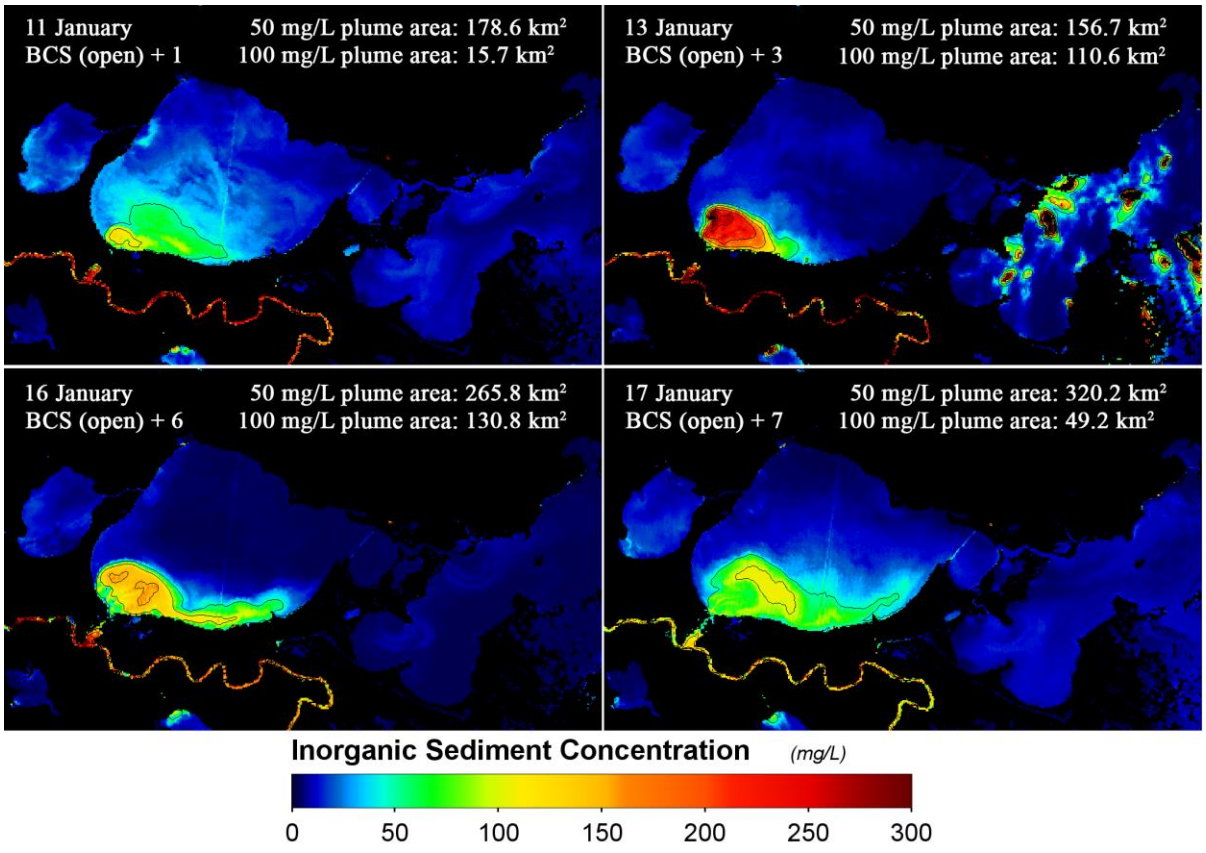

Figure 6.3: Inorganic sediment concentration (mg L^{-1}) for 11, 13, 16, and 17 January. Contour lines separate concentrations every 50 mg L^{-1} from 0 mg L^{-1} (blue) to 300 mg L^{-1} (dark red).

The easternmost point of the 50 mg L^{-1} isopleth actually regressed westward about 6 km by 13 January. The plume then traveled eastward to a point 36 km from the Spillway mouth by 16 January and traveled an additional 4 km by the following day. From these observations, the average eastward speed of motion was calculated as ~1 km h^{-1} (or 0.3 m s^{-1}) for the first week of the Spillway opening from 11 January to 17 January.

By 17 January, the leading edge of the Mississippi River material, which was beyond the 50 mg L^{-1} isopleth edge, had traveled eastward 50 km while hugging the southern coastline of the Lake and nearly reaching the Twin Span bridge. The highest concentration area of the plume, however, moved in a general northeastward direction, rather than eastward, but only progressed to approximately 15 km from the Spillway mouth in the 11 – 17 January timeframe. The 50 mg L^{-1} plume was distributed across nearly 20% of the total Lake Pontchartrain area by 17 January; whereas the highest areal distribution of the 100 mg L^{-1} plume in this first week of the diversion was ~8% of the Lake's area, as observed on 13 January (Figure 6.4).

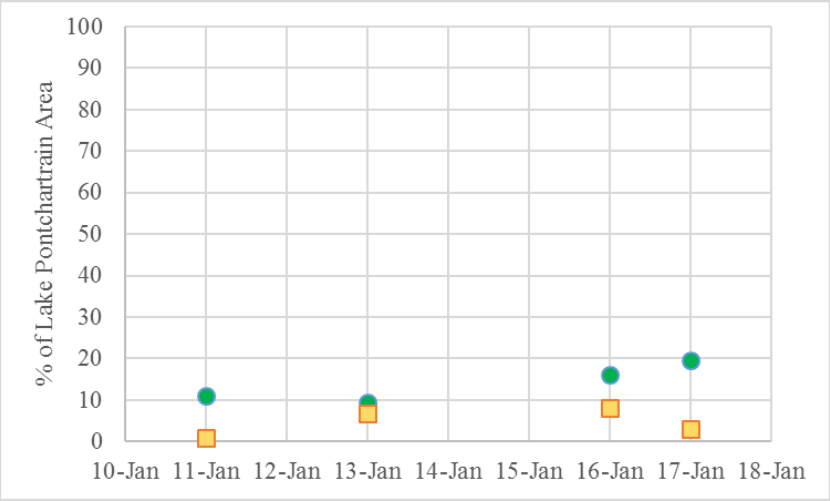

Figure 6.4: 50 mg L^{-1} (green points) and 100 mg L^{-1} (yellow squares) inorganic sediment concentration plume areas as a percentage of total Lake Pontchartrain area

Figure 6.5 depicts the sediment plume dispersal in the second week following the BCS opening: 18, 19, 23, and 24 January. The trend of northeastward motion of the high

concentration areas continued, but the size and mean concentration of these areas were greatly increased as compared to the first week of the diversion event. The area of lower mean sediment concentration continued to move eastward along the southern Lake Pontchartrain coast. For 18 and 19 January, the highest sediment concentration was found in the south central portion of the Lake; by 23 and 24 January, the highest concentrations were evenly distributed across the central area of the Lake.

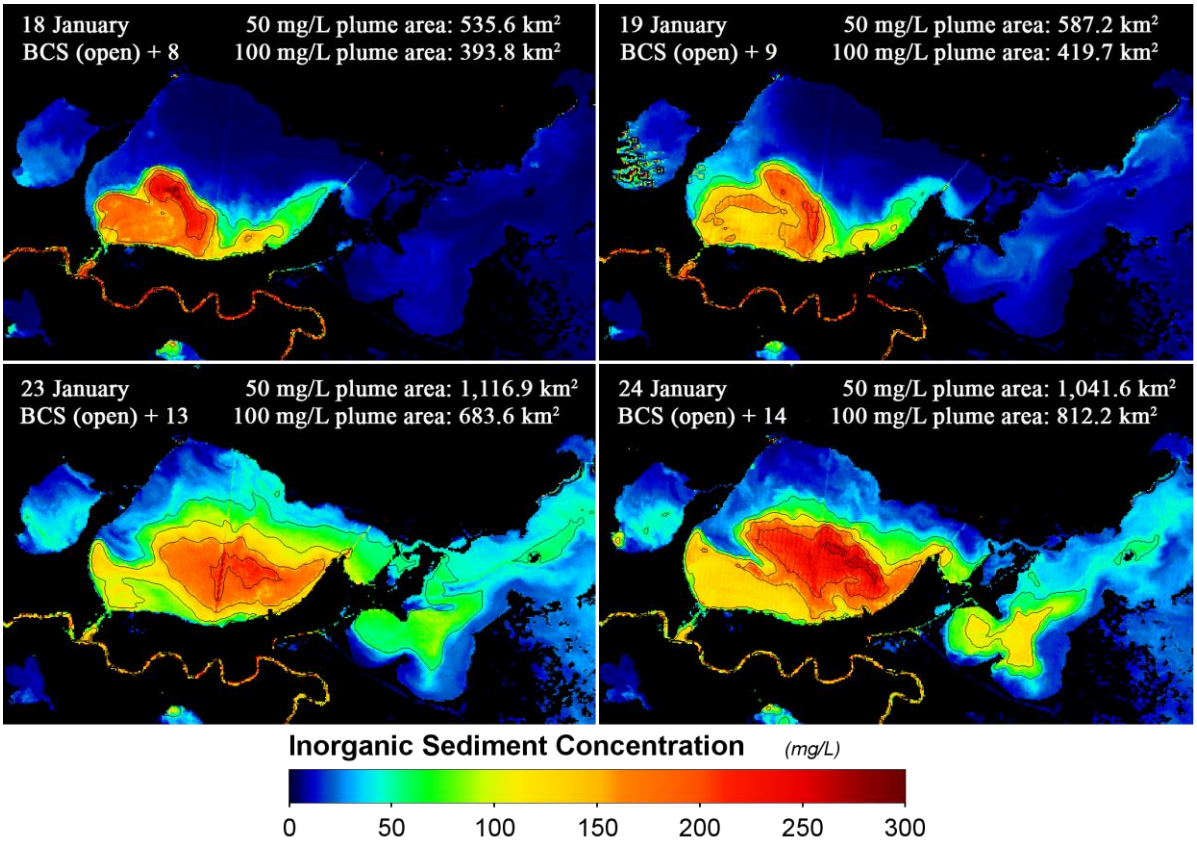

Figure 6.5: Inorganic sediment concentration (mg L^{-1}) for 18, 19, 23, and 24 January. Contour lines separate concentrations every 50 mg L^{-1} from 0 mg L^{-1} (blue) to 300 mg L^{-1} (dark red).

The size of the 50 mg L^{-1} ISC plume nearly doubled (from ~587 km^2 to ~1,117 km^2) in the four days from 19 to 23 January. As a percentage of the total Lake area, the 50 mg L^{-1} ISC plume reached its peak (68%) for the entire event on 23 January, a sharp increase from the 36% coverage observed on 19 January. The 100 mg L^{-1} ISC plume increased in size by 263 km^2 in the

same four day period with an additional 128 km^2 growth from 23 to 24 January. The 100 mg L^{-1} ISC plume area growth was also significant for this timeframe, increasing from 26% of the total Lake area to 50% from 19 to 24 January (Figure 6.6).

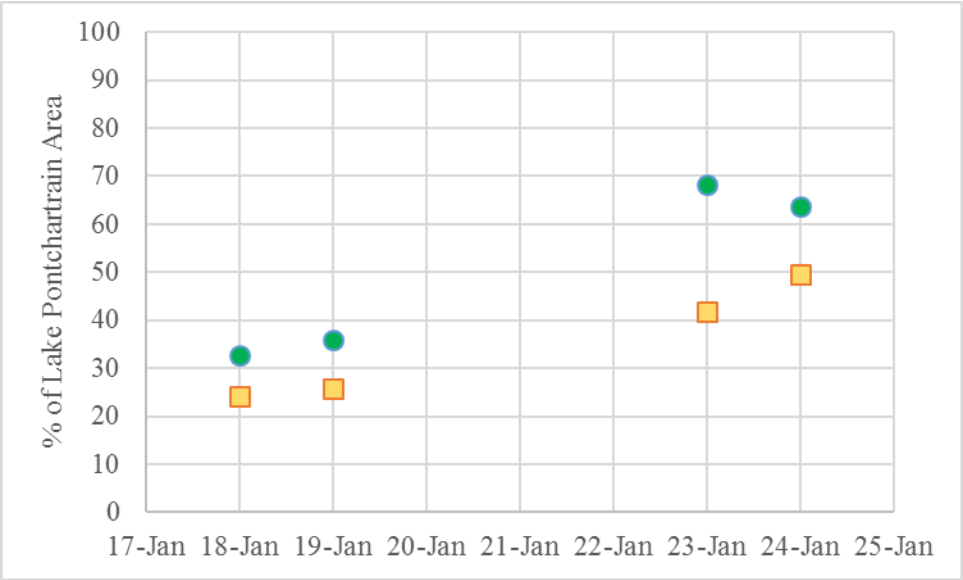

Figure 6.6: 50 mg L^{-1} (green points) and 100 mg L^{-1} (yellow squares) inorganic sediment concentration plume areas as a percentage of total Lake Pontchartrain area

Up to 19 January, the overall plume motion had been oriented in a mostly eastward or northeastward direction away from the Spillway mouth. The first hints of any significant movement of the sediment plume in the far western portion of the Lake began on 19 January as a portion of the plume migrated northwest approximately 5 km between 18 and 19 January. By 23 January, the plume was more clearly advancing northward along the western coast of the Lake, traveling just over 4 km northward from 23 to 24 January, while the rest of the plume continued to move eastward and northeastward.

Satellite observations indicate that the leading edge of the Mississippi River sediment plume entered Lake Borgne between 18 and 19 January. The surface sediment took the narrower path through the Chef Menteur Pass as opposed to through the wider Rigolets channel. River gage data revealed a higher water elevation at the Rigolets station, 0.14 m and 0.6 m for 18 and

19 January, respectively. The Chef Menteur Pass water elevation was recorded at 0.08 m and 0.3 m for those same dates. There, the lower water levels at Chef Menteur Pass enhanced discharge of Mississippi River water before reaching the Rigolets channel, 11 km to the northeast. By 23 January, however, imagery revealed that the plume water had begun to flow through the Rigolets as well, although surface sediment transport through Chef Menteur Pass appeared to remain more pronounced for 23 and 24 January.

Figure 6.7 depicts the time history from 28 and 29 January as well as 5 and 7 February. The daily discharge rate of the Spillway had been under a period of controlled reduction since 24 January, but the areas of high sediment concentration persisted. In fact, the 100 mg L^{-1} ISC plume reached its peak areal distribution, of 905 km^2, on 29 January when the spillway discharge was 30% of its observed peak daily discharge. A noted area of low sediment concentration, extending southeastward toward the Lake center from the northwest, appeared to bisect the sediment plume, behavior which could possibly be attributed to high discharge from the Tangipahoa River. Tangipahoa discharge at USGS station #7375500, located approximately 35 km upriver from Lake Pontchartrain, increased from 20 $m^3 s^{-1}$ on January 20 to 52 $m^3 s^{-1}$ on 23 January. It is possible that the increased Tangipahoa discharge waters observed at the Robert station did not reach the Lake until these later image dates given the station's distance from the Lake. The 28 and 29 January images also showed the first signs of westward movement of the plume in the northeastern portion of the Lake which may be evidence of the Coriolis effect impacting the motion of the sediment-laden water and/or effects of the incoming tide through the Rigolets.

The 5 and 7 February images are the first clear-sky images available after the closing of the Spillway. Despite the cessation of sediment influx into the Lake, the 50 mg L^{-1} sediment

plume maintained a large spatial distribution through 7 February. The 100 mg L^{-1} plume, however, collapsed by 30% of its areal size from 29 January to 5 February, a reduction from 54% to 32% of overall Lake Pontchartrain area (Figure 6.8).

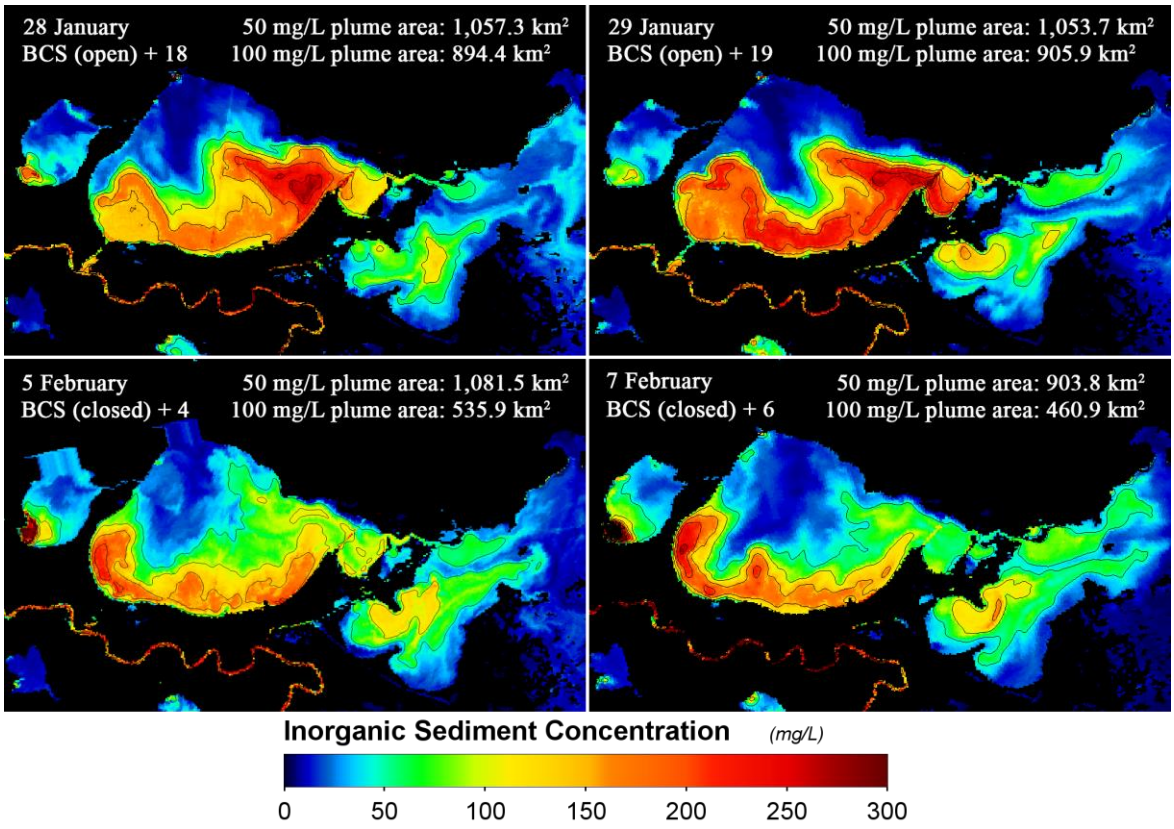

Figure 6.7: Inorganic sediment concentration (mg L^{-1}) for 28-29 January; 5 and 7 February. Contour lines separate concentrations every 50 mg L^{-1} from 0 mg L^{-1} (blue) to 300 mg L^{-1} (dark red).

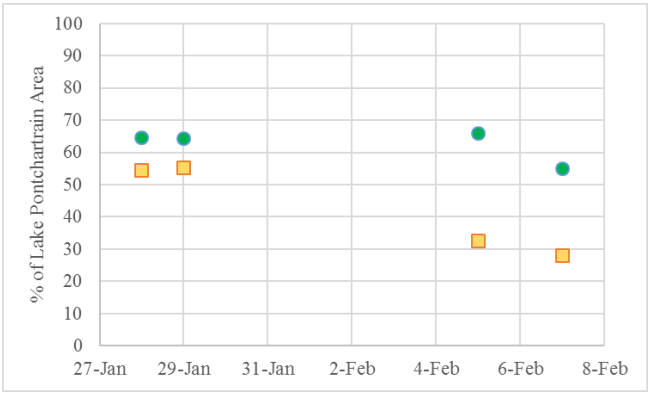

Figure 6.8: 50 mg L^{-1} (green points) and 100 mg L^{-1} (yellow squares) inorganic sediment concentration plume areas as a percentage of total Lake Pontchartrain area

The plume morphology did not change greatly from 28 January to 7 February, as the plume maintained its position nearly exclusively along the southern coastline of the Lake. However, after the Spillway closure, the area of highest sediment concentration was found in the westernmost portion of the Lake. The northward movement of this western tongue of the plume, as observed on 23 and 24 January, appeared to have regressed by 28 January. A slight subsequent increase in northward displacement of the western plume arm on 29 January was followed by significant gains in northward movement. The 50 mg L^{-1} plume exhibited a 13 km displacement from 29 January to 5 February and the 100 mg L^{-1} plume exhibited displacement of 6 km from 5 to 7 February.

Figure 6.9 depicts images from 8, 10, 11, and 17 February. By 8 February, the Mississippi River sediment had dispersed throughout nearly the entirety of Lake Pontchartrain, so from that date onward, no plume areas were calculated. The northward motion of the western arm of the plume, as observed on 23, 24, and 29 January and 5 and 7 February, appeared to continue on 8 February although the sediment concentrations of both the western arm, and the plume as a whole, were greatly reduced as compared to 7 February. A marked increase in overall sediment concentration across the Lake was observed throughout the period from 8 to 11 February, on which day the overall mean ISC for the entirety of Lake Pontchartrain reached its peak observed value for this study: approximately 133 mg L^{-1}. The highest areas of ISC were found in the southeast portion of the Lake on 10 and 11 February.

A significant collapse in the sediment plume's size and mean concentration occurred from 11 to 17 February. Very little Mississippi River sediment remained, in a suspended state, by 17 February and only a fraction of that sediment appeared to be exiting the Lake through the Chef Menteur Pass and Rigolets channel by that date. The mean sediment concentration of Lake

Pontchartrain rapidly decreased from approximately 133 mg L^{-1} to 36 mg L^{-1} between 11 and 17 February. The 17 February mean Lake Pontchartrain ISC value was the lowest observed mean Lake ISC since 17 January, on which day the mean Lake ISC was 27 mg L^{-1}.

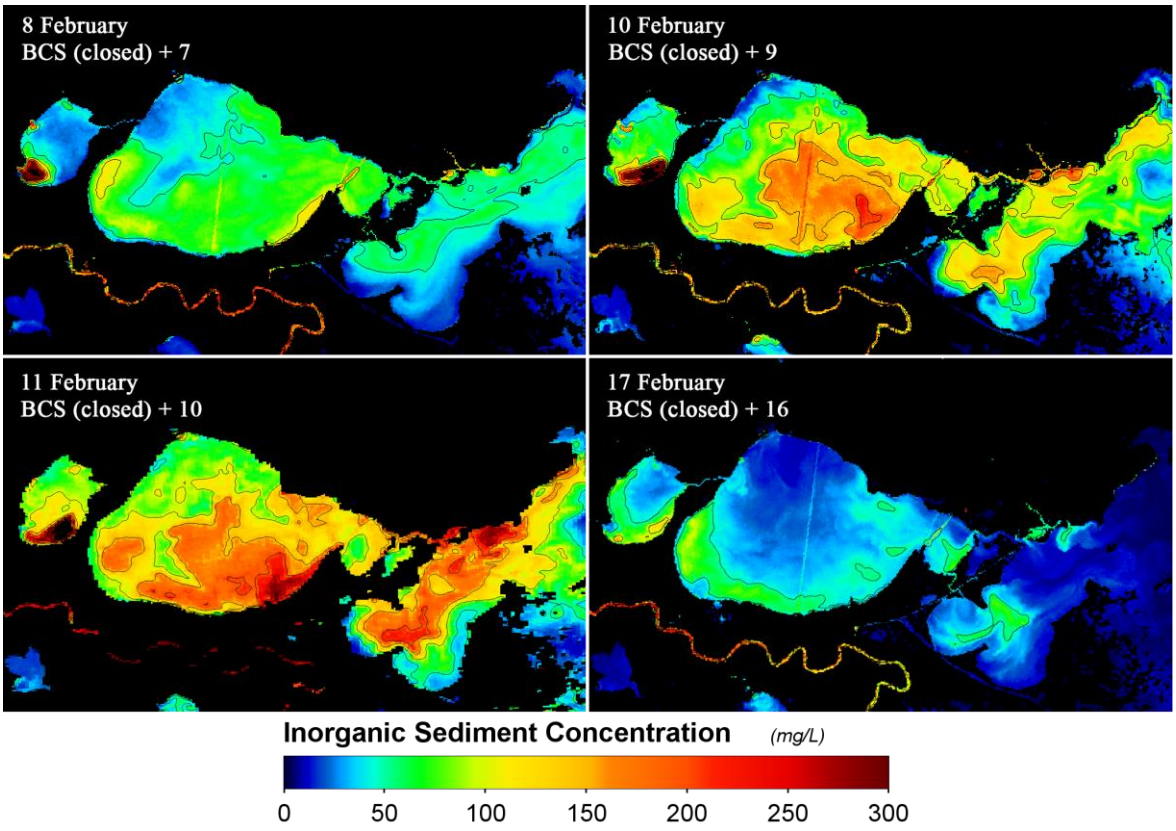

Figure 6.9: Inorganic sediment concentration (mg L^{-1}) for 8, 10, 11, 17 February. Contour lines separate concentrations every 50 mg L^{-1} from 0 mg L^{-1} (blue) to 300 mg L^{-1} (dark red).

Figure 6.10 contains imagery for 18, 25, 26, and 27 February, the final dates of imagery processed for the 2016 diversion event. The 18 February plume demonstrates a similar morphology to that of the 17 February image, with the highest ISC on the southwestern coastline of the Lake. Again, an arm of the 50 mg L^{-1} plume climbed northward along the western coastline, traveling a distance of 10 km from 17 to 18 February.

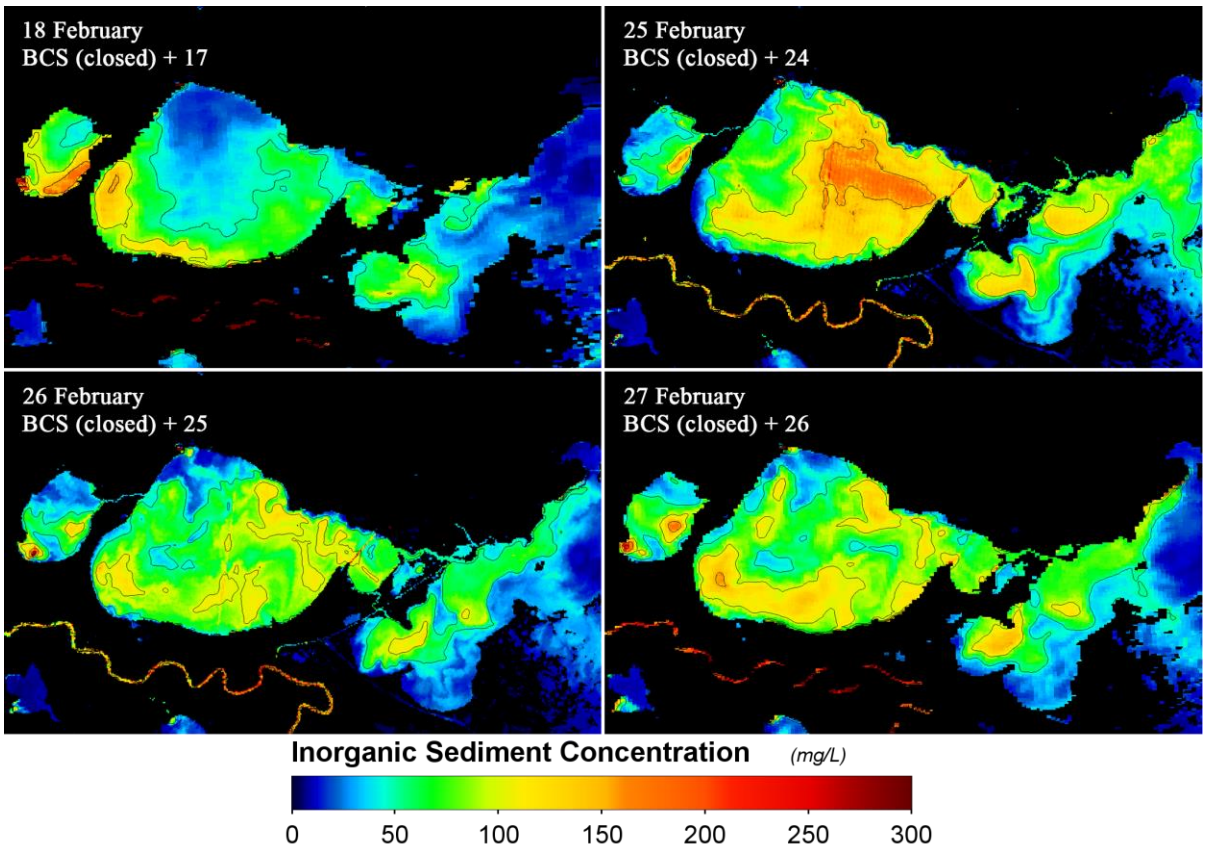

Figure 6.10: Inorganic sediment concentration (mg L^{-1}) for 18, 25, 26, and 27 February. Contour lines separate concentrations every 50 mg L^{-1} from 0 mg L^{-1} (blue) to 300 mg L^{-1} (dark red).

A massive shift in plume morphology and in the location of highest sediment concentration was observed from 18 to 25 February. Whereas the plume was hardly discernible on 17 February and only marginally increased in size by 18 February, the entire lake was again flush with surface suspended sediment material by 25 February. The high sediment regime persisted through 27 February although the area of highest concentration in the eastern Lake disappeared in that timeframe, but strengthened in the southwestern portion of the Lake.

6.2.3 Impacts of Wind Resuspension on Plume Area

Section 6.2.2 noted that the movement of the sediment plume could have been attributed to the Coriolis effect in some cases. However, vast changes in sediment plume morphology and mean concentration were observed between various date ranges; changes which may not be

easily explained by Coriolis, tributary discharge, or water level, but rather by winds. White et al. (2009) observed for the 2008 BCS diversion event and Roy et al. (2013) for the 2011 event that the eastward movement of the plume along the southern Lake Pontchartrain coastline could be explained by the Coriolis effect. However, their studies also noted that winds have the potential to interrupt said effects. Walker (1996) identified winds as the primary driver of daily and smaller-scale changes in sediment plume morphology and concentration for Mississippi River sediments entering the Gulf of Mexico through the bird-foot delta region. Booth et al. (2000), in a study of Barataria Bay, found that winds of various magnitude were responsible for resuspending different percentages of bottom sediments: 4 m s^{-1} resuspended 50% of bottom sediments and 10 m s^{-1} resuspended 80% of bottom sediments. However, the sediment observed in the 2016 BCS diversion may not necessarily be of like composition to those of the Booth et al. (2000) study. The wind values reported by Booth et al. (2000) for resuspension are, therefore, treated as a guideline for potential resuspension of Mississippi River sediment in Lake Pontchartrain rather than concrete threshold values. This section explores whether select observations from Section 6.2.2 can be linked to changes in wind speed and direction. Winds in this section are discussed in the meteorological convention.

Figures 6.11 and 6.12 contain wind speed and direction data for the MSY station from 18 through 24 January. From 19 to 23 January, the 50 mg L^{-1} plume area nearly doubled in size (from 587 km^2 to 1,116 km^2). Wind speeds in the 24 hours prior to 18 and 19 January image collection were weak, averaging 3.2 m s^{-1} and 1.9 m s^{-1}, respectively. Plume areal size for those dates was likely a function primarily of BCS discharge and the Coriolis effect. However, wind speeds increased greatly in the period from 21 to 23 January with speeds ranging between 0 and 3 m s^{-1} on 21 January to ~10-12 m s^{-1} on 22 January. The higher wind speeds in that timeframe

likely contributed to increased water column and/or bottom sediment resuspension, resulting in the large increase in plume area observed on 23 January. The slight decrease in 50 mg L^{-1} plume area for 24 January could be explained by the reduction in wind speed from 23 to 24 January. It is interesting to note that the 100 mg L^{-1} plume area increased, rather than decreased, between 23 January and 24 January (683 km^2 to 812 km^2).

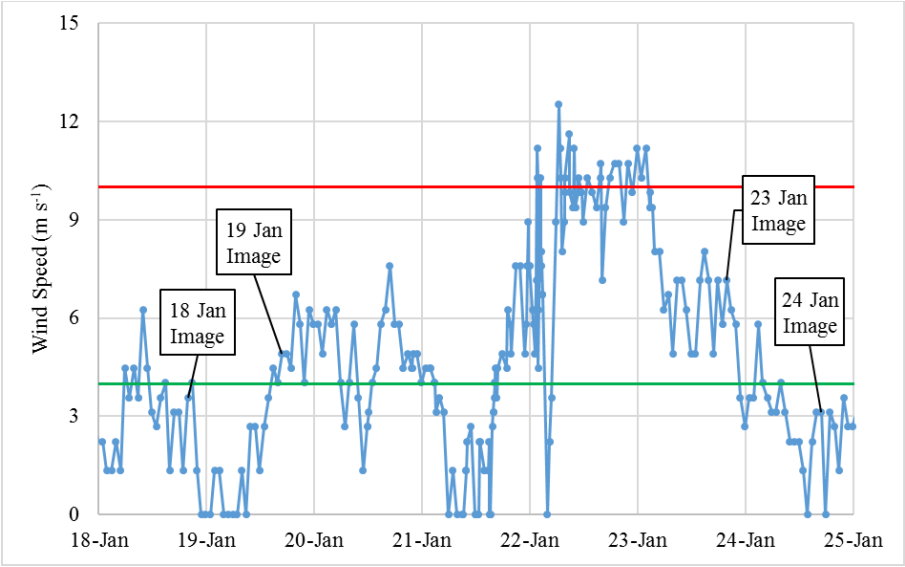

Figure 6.11: Wind speed (m s^{-1}) at MSY for 18 to 24 January. Green and red lines represent the Booth et al. (2000) sediment resuspension thresholds of 4 m s^{-1} and 10 m s^{-1}, respectively.

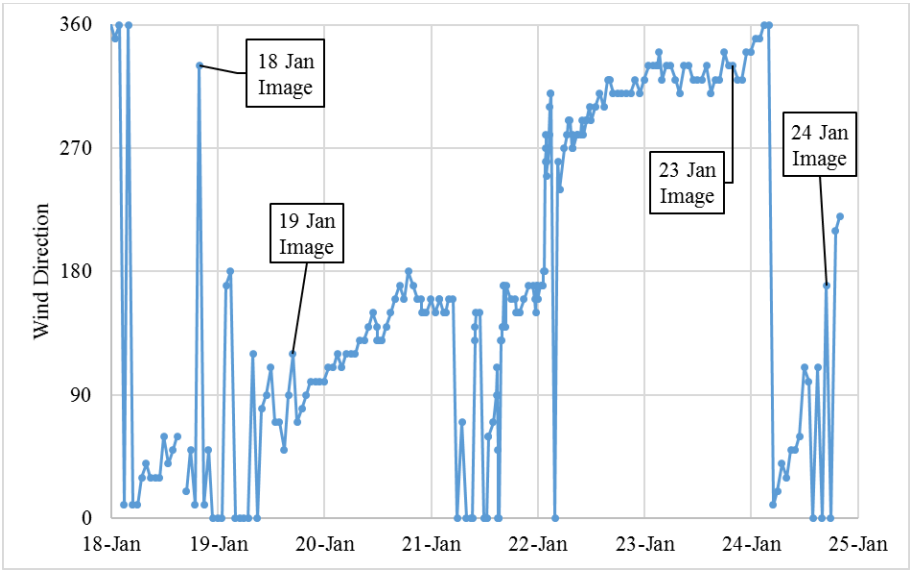

Figure 6.12: Wind direction at MSY for 18 to 24 January

Figures 6.13 and 6.14 contain wind speed and direction data for the MSY station for 28 and 29 January. From 28 to 29 January, both the 50 mg L^{-1} and 100 mg L^{-1} plume areal distributions remained mostly unchanged, which is not unusual given that wind speeds for the 24-hr period prior to 28 January averaged 5 m s^{-1} and, for the 29 January 24-hr period, only 3.3 m s^{-1}.

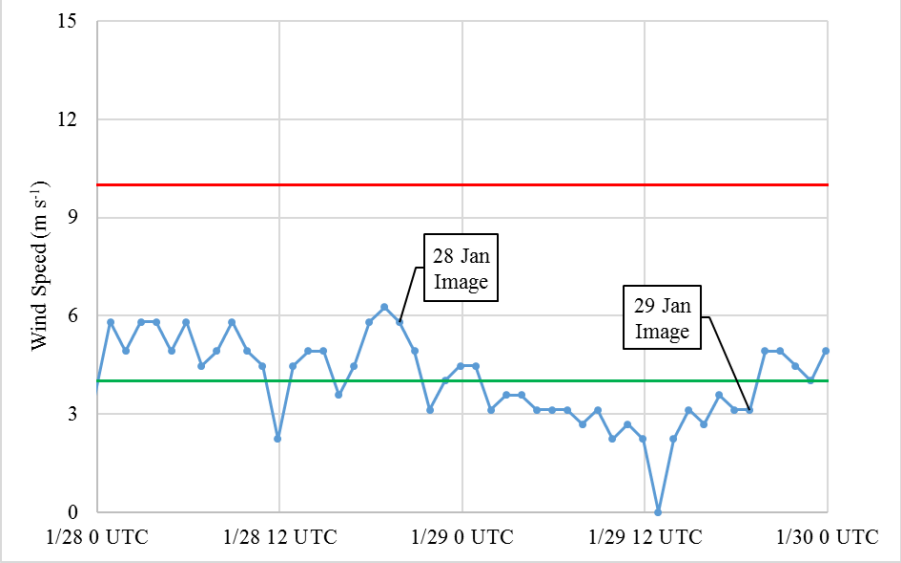

Figure 6.13: Wind speed (m s^{-1}) at MSY for 28 and 29 January. Green and red lines represent the Booth et al. (2000) sediment resuspension thresholds of 4 m s^{-1} and 10 m s^{-1}, respectively.

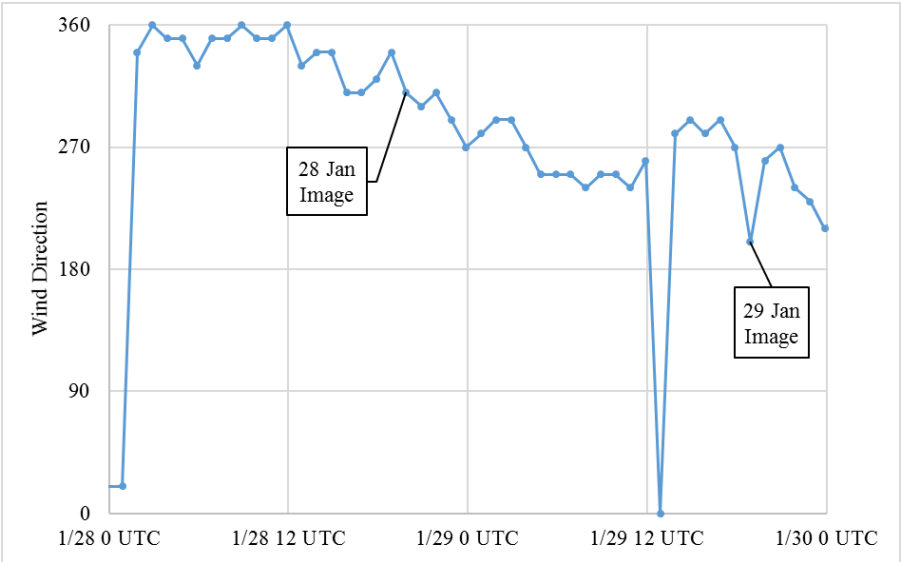

Figure 6.14: Wind direction at MSY for 28 and 29 January.

A large tongue of lower sediment water, moving southward, appeared to cut into the Mississippi River sediment plume on 28 and 29 January. As noted in Section 6.2.2, this lower sediment concentration water may have been associated with an increase in Tangipahoa River discharge in the days prior. Winds were sustained out of the north and northwest prior to and on 28 January and out of the west prior to 29 January (Figure 6.14), both observations could help to explain the southward movement of the lower ISC water. These observations could have aided the apparent counter-clockwise motion typically produced by the Coriolis effect.

Figures 6.15 and 6.16 contain wind speed and direction data for the MSY station for 5 through 7 February. The BCS closed on 1 February, but the 50 mg L^{-1} plume area on 5 February was slightly increased from that of 29 January. North and northeast winds averaged 6 m s^{-1} in the 24 hour period prior to 5 February image collection.

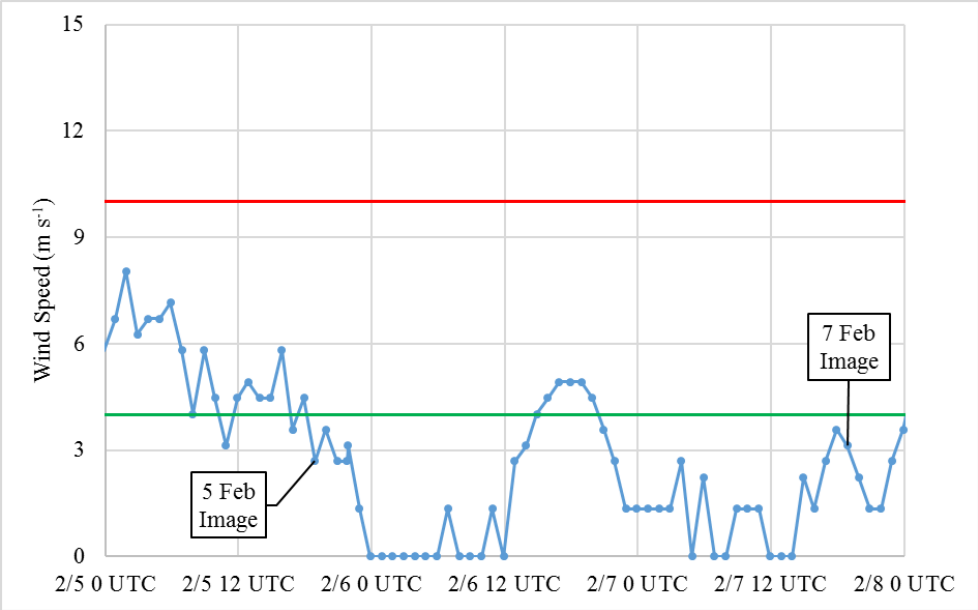

Figure 6.15: Wind speed (m s^{-1}) at MSY from 5 to 7 February. Green and red lines represent the Booth et al. (2000) sediment resuspension thresholds of 4 m s^{-1} and 10 m s^{-1}, respectively.

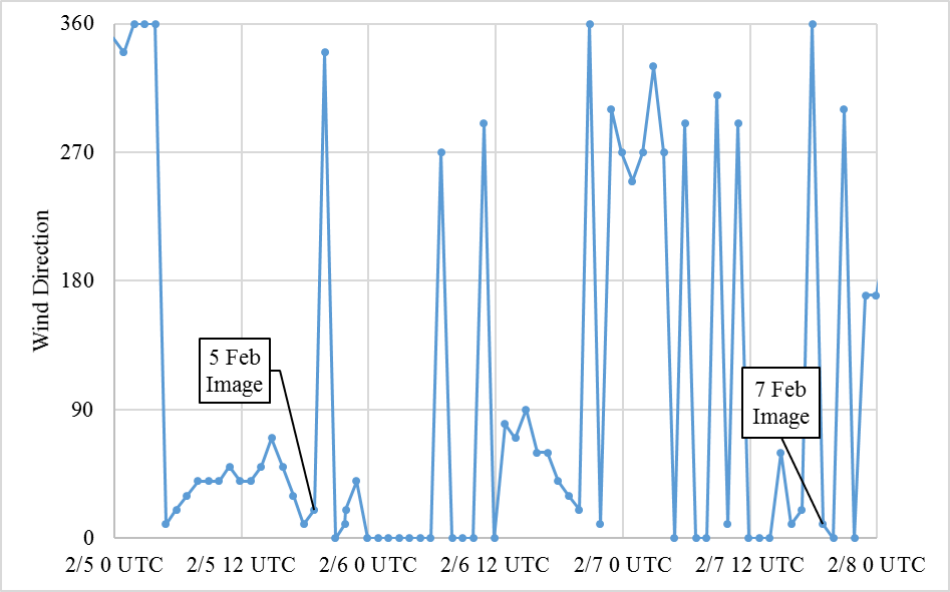

Figure 6.16: Wind direction at MSY from 5 to 7 February.

Wind-induced sediment resuspension may have helped to sustain the 50 mg L^{-1} plume area even without any new sediment from the BCS. However, the 100 mg L^{-1} area decreased in size by 30% from 29 January to 5 February, perhaps because wind speeds were not high enough to sustain the higher concentration of sediment. Wind speeds were further reduced between 5 and 7 February, averaging just 1.7 m s^{-1} for the 24 hour period prior to 7 February, and were erratic in direction. The observation of reduced wind speed from 5 to 7 February may help to explain the reduction in both 50 mg L^{-1} and 100 mg L^{-1} plume areas, but neither the wind speed, erratic wind direction, nor Coriolis may necessarily explain the northward motion of the 100 mg L^{-1} plume along the western Lake Pontchartrain coastline, which may have been a response to southward motion of the lower sediment water from the Tangipahoa or other tributaries.

Although the 100 mg L^{-1} plume had all but disappeared by 8 February, the 50 mg L^{-1} plume grew from 7 February to cover nearly the entire Lake by 8 February. Steadily increasing winds, averaging 5 m s^{-1} in the 24 hour period prior to 8 February (Figure 6.17) and measuring over 12 m s^{-1} at image collection time on 8 February, likely help to explain the apparent

resuspension and surface plume enlargement that occurred between 7 and 8 February. Westerly winds prior to 8 February (Figure 6.18) may explain the larger area of suspended sediment in the eastern portion of the Lake.

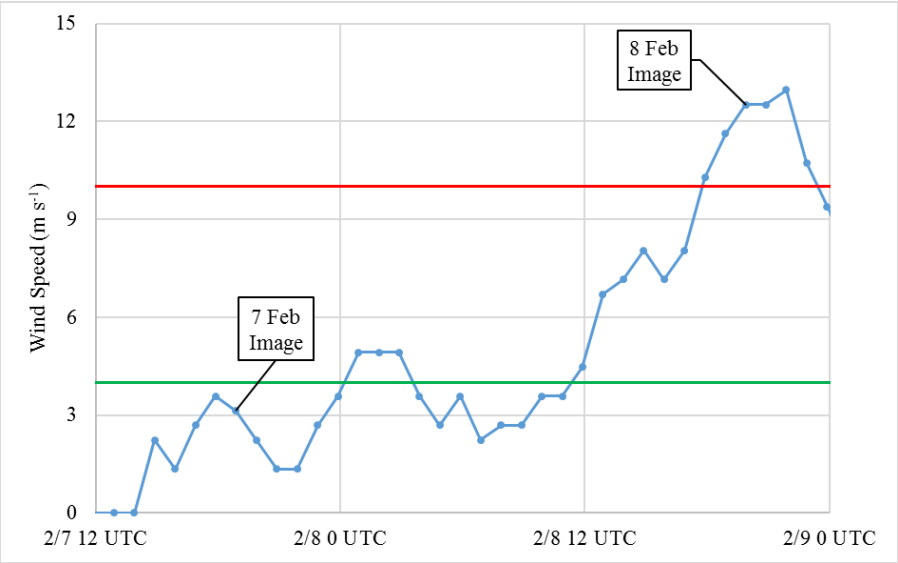

Figure 6.17: Wind speed (m s^{-1}) at MSY from 7 to 9 February. Green and red lines represent the Booth et al. (2000) sediment resuspension thresholds of 4 m s^{-1} and 10 m s^{-1}, respectively.

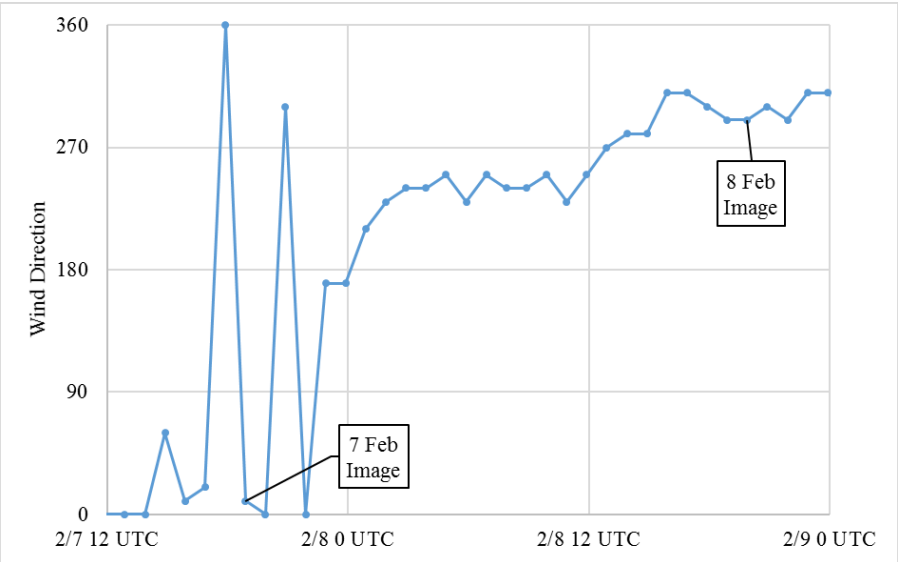

Figure 6.18: Wind direction at MSY from 7 to 9 February.

After image acquisition on 8 February, wind speeds decreased on 9 February to below 9 m s^{-1} with a slight rebound above 10 m s^{-1} late that day (Figure 6.19). Although wind speeds

were relatively low (< 4 m s^{-1}) on 10 February, the high wind speeds during the previous days may explain the large amount of sediment resuspension observed between 8 and 10 February. Additionally, it is possible that the surface sediment plume did not necessarily settle out quickly once resuspended. Wind speeds averaging 4.5 m s^{-1} and peaking around 8 m s^{-1} prior to the 11 February image could help to explain the additional increase in ISC from 10 to 11 February.

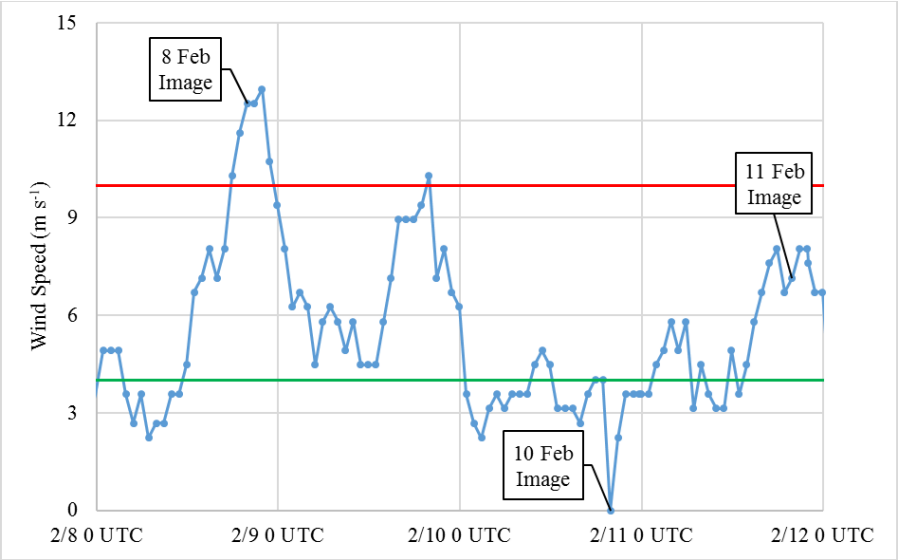

Figure 6.19: Wind speed (m s^{-1}) at MSY from 8 to 11 February. Green and red lines represent the Booth et al. (2000) sediment resuspension thresholds of 4 m s^{-1} and 10 m s^{-1}, respectively.

The location of the highest sediment concentration appeared to be located in the central and southeastern portions of the Lake on both 10 and 11 February. This may be explained by the observed west-northwest winds that prevailed in the days preceding the 10 February image collection (Figure 6.20). The winds switched to south-southwest shortly before 11 February image collection, perhaps explaining the greater ISC observed in the northern Lake Pontchartrain waters as compared to the 10 February image.

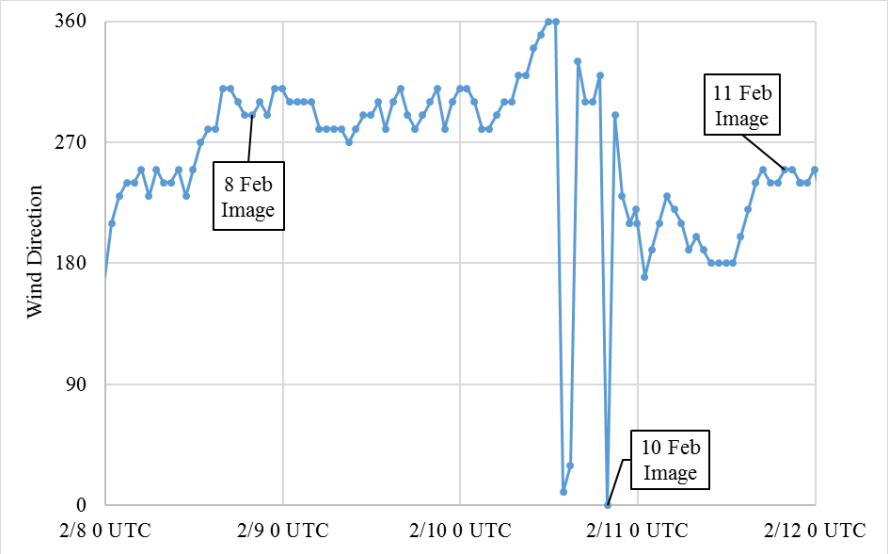

Figure 6.20: Wind direction at MSY for 8 to 11 February.

Wind speeds varied in the period from 11 to 17 February, but averaged a weak 4.4 m s^{-1} in the 24 hour period prior to the 17 February image collection (Figure 6.21). This observation may help to explain the observed sharp collapse in mean Lake Pontchartrain sediment concentration in this timeframe. The BCS had been closed for over two weeks by the 17 February observation, which may indicate that, the further away in time from the diversion event, the more influential other factors, in addition to winds and Spillway discharge, become. The wind speed variable itself may not be enough to explain the plume variability from 11 to 17 February, but the observed erratic wind direction in the 24 hours prior to 17 February image collection may provide a clue (Figure 6.22). Perhaps a sustained wind from one direction is necessary for a certain period of time in order to successfully resuspend sediment. Since no such prevailing winds were observed in the 24 hour period for 17 February, that may explain the relatively low observed sediment concentration.

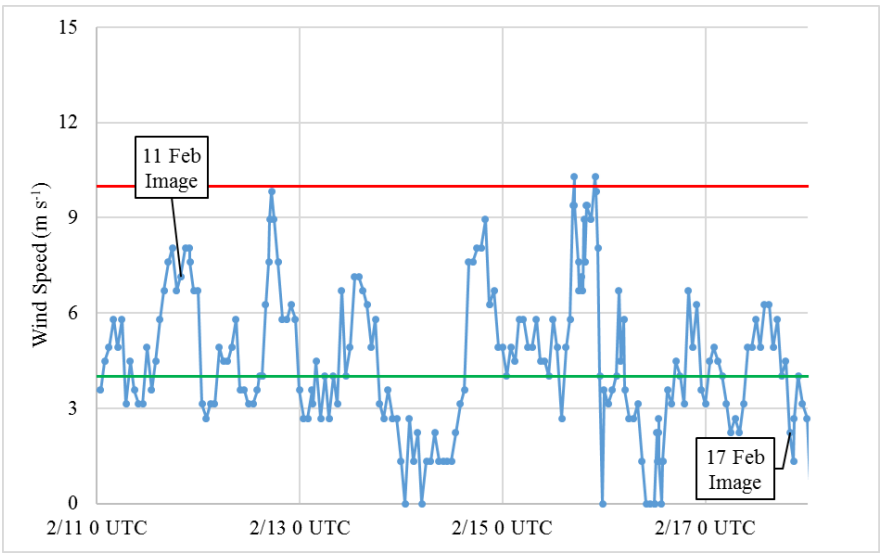

Figure 6.21: Wind speed (m s^{-1}) at MSY from 11 to 17 February. Green and red lines represent the Booth et al. (2000) sediment resuspension thresholds of 4 m s^{-1} and 10 m s^{-1}, respectively.

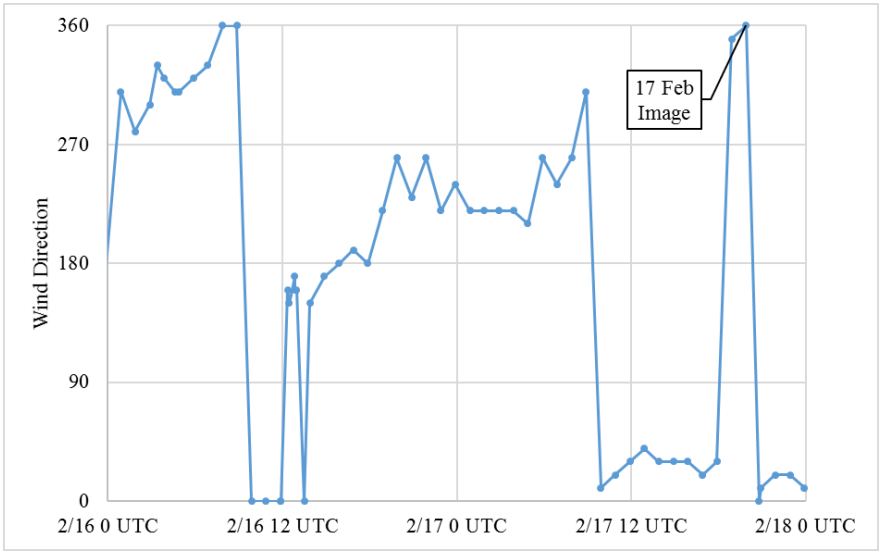

Figure 6.22: Wind direction at MSY for 16 and 17 February.

Wind speed and direction data from the MSY station for 24 to 27 February are shown in Figures 6.23 and 6.24, respectively. Winds averaged 5 m s^{-1} in the 24 hour period prior to the 25 February image collection, but averaged over 8 m s^{-1} in the 48 hour period, which can possibly explain the significant resuspension of sediment observed from 18 to 25 February. The mean Lake sediment concentration decreased from 108 mg L^{-1} on 25 February to 84 mg L^{-1} by 27

February, possibly owing to the reduction in wind speed in that timeframe. Winds averaged just 1.5 m s^{-1} prior to 27 February image collection.

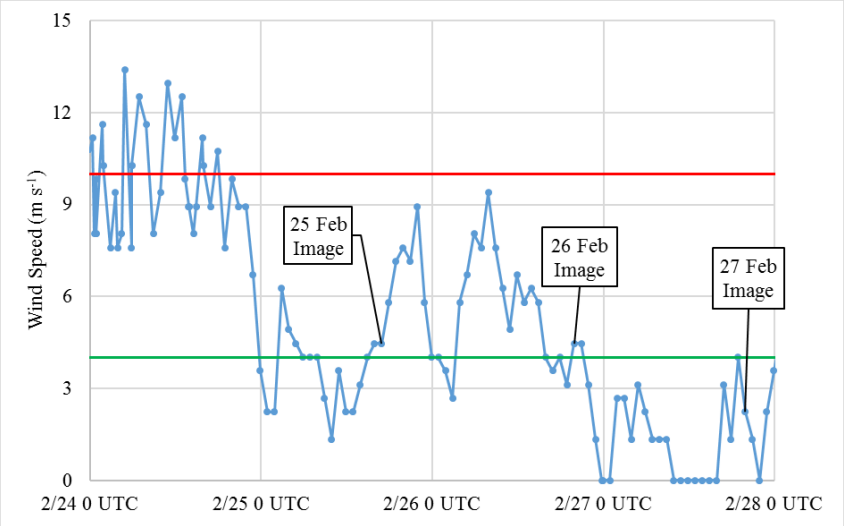

Figure 6.23: Wind speed (m s^{-1}) at MSY from 24 to 27 February. Green and red lines represent the Booth et al. (2000) sediment resuspension thresholds of 4 m s^{-1} and 10 m s^{-1}, respectively.

A strong westerly wind prior to 25 February image collection helps to explain the large area of high sediment concentration present in the eastern portion of the Lake for that day. Weak, erratic winds thereafter may explain the lack of any one defined area of highest sediment concentration for 26 and 27 February.

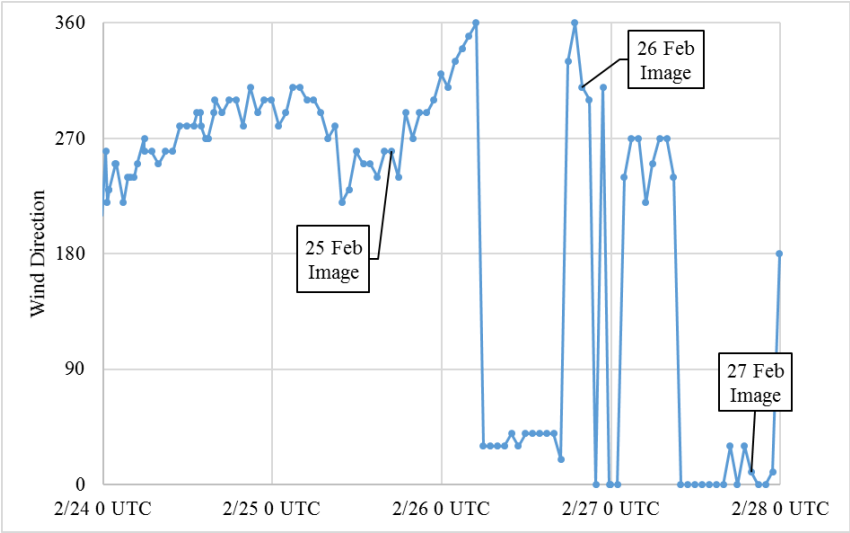

Figure 6.24: Wind direction at MSY for 24 to 27 February.

6.2.4 Discussion

Chapter 6 has demonstrated a practical use of satellite remote sensing methods for detecting and tracking the spatial and temporal variability of the Mississippi River sediment plume in Lake Pontchartrain. The sediment plume, introduced into the Lake via the BCS, was investigated using a series of twenty satellite images ranging in date from 11 January to 27 February 2016. The images were processed to determine ISC (in mg L^{-1}) according to methods described in Chapters 4 and 5. In Chapter 4, comparison of field spectroradiometer measurements from 13 March 2016 and satellite reflectance values, derived using the CWP method for aerosol correction of Rayleigh-corrected imagery, yielded an average error of 0.4%.

The sediment plume area appeared to be controlled initially by daily BCS discharge rates. The 50 mg L^{-1} plume area increased steadily with daily BCS discharge, with an approximate three day lag. The 100 mg L^{-1} plume area also increased with increasing BCS daily discharge, albeit with less apparent correlation and with a greater lag of approximately five days. The 50 mg L^{-1} plume remained steadily high until after 7 February, even after the period of reduction in daily BCS discharge from 24 to 31 January. The 100 mg L^{-1} plume experienced a ~50% decrease in area within the four days following Spillway closure.

In the month following Spillway closure, the sediment plume morphology varied greatly between image observations. With no continued input from the Spillway, such variability would likely have been due to other factors. Given the high observed variance between the 50 mg L^{-1} and 100 mg L^{-1} isopleths' spatial areas following the Spillway closure, daily winds and Lake Pontchartrain tributary discharge were examined in detail as possible additional forcing factors for the observed sediment plume variability.

In the first week of the diversion opening, the plume moved along the southern coastline, consistent with a general counter-clockwise circulation of Lake waters, as has been observed in prior diversion events (White et al. 2009; Roy et al. 2013). The general movement of the plume could be explained by the Coriolis effect in some cases, but was at other times interrupted by changes in daily winds. Periods of increasingly strong winds from 19 to 24 January, 7 to 8 February, and 18 to 25 February corresponded to significant increases in plume area and mean ISC for those date ranges. Similarly, reduced winds from 29 January to 5 February may explain observed decreases in plume area for that timeframe.

Similar to plume area, the location of highest sediment concentration was at first explained by BCS daily discharge rate at the beginning of the diversion event. However, wind direction became seemingly more impactful in determining the highest area of sediment concentration even before Spillway closure: northwesterly winds prior to 23 and 24 January may have resulted in the dispersal of high sediment concentrations across the center of the Lake from northwest to southeast. On 10 and 11 February, after periods of west and northwest winds, the plume was observed to have the highest sediment concentration in the southeast portion of the Lake; strong westerly winds likely resulted in the observed area of highest concentration in the easternmost portion of the Lake. North and west-northwest winds also may have played a role in moving waters of lower sediment concentration in a southeast direction, bisecting the sediment plume in the center of the Lake from 28 to 29 January.

The Mississippi River sediment plume, moving at ~1 km h^{-1} (0.3 m s^{-1}), appeared to first exit Lake Pontchartrain between 18 and 19 January, eight days after the opening of the Spillway. The sediment first exited via the narrower Chef Menteur Pass as opposed to the wider Rigolets channel, behavior that was perhaps explained by the prevailing easterly and northerly winds that

prevailed on 18 and 19 January, respectively. Water level, which was measured higher at the Rigolets gage station, also likely played a critical role enhancing sediment transport through the Chef Menteur Pass. By 23 January, sediment-laden water was flowing through both channels, behavior that mostly continued throughout the rest of the observations into late February.

The behavior of the 2016 BCS sediment plume was similar to observations made during previous BCS diversion events in 2008 (White et al. 2009) and 2011 (Roy et al. 2013). As with the 2016 event, both previous events observed eastward plume motion along the southern Lake Pontchartrain coastline. The maximum 50 mg L^{-1} plume area for the 2016 event, approximately 1,117 km^2, was slightly less than the 1,200 km^2 observed in the 2011 event, but greater than the 616 km^2 of 2008 (Roy et al. 2013), although no distinction between areas of different sediment concentrations was made for those events as with the 2016 event. The 2016 event was unique in the fortunate abundance of clear-sky high quality MODIS satellite imagery for this study while images from both the 2008 and 2011 events were plagued by sunglint and cloud issues. The problem of sunglint in satellite imagery of this region becomes more prevalent in the spring and summer months. Additional cloud-free images were available for the 2016 event from the MODIS Terra sensor, but most were not used because the newly developed ISC model was valid only for MODIS Aqua images.

CHAPTER 7: SUMMARY AND CONCLUSIONS

This project involved the use of field measurements of sediment concentration, spectroradiometer reflectance measurements, and MODIS satellite images to characterize the movement and fate of Mississippi River sediments introduced into Lake Pontchartrain via the BCS during the 2016 river flood and diversion event. The research questions investigated by this study were answered in the following ways:

1) Standard NASA aerosol correction methods, designed for Case 1 waters, mistook the areas of high turbidity present in Lake Pontchartrain for clouds and yielded erroneous reflectance values, which necessitated a manual approach to aerosol correction of the MODIS imagery. Aerosol correction was successfully accomplished using the CWP method applied to Rayleigh-corrected imagery. Spectroradiometer data collected on 13 March was critical for assessing the success of this technique. Although there were a low number of data points available for the validation of the CWP using field spectroradiometer data (n = 8), the results suggest that the CWP method was an effective technique for aerosol correction of MODIS imagery during the 2016 BCS diversion event in Lake Pontchartrain, with an average error of 0.4%. Future studies would benefit from increased field sites across different days and in different seasons to ascertain the CWP method's effectiveness as an aerosol correction technique for Lake Pontchartrain in varying environmental and atmospheric conditions.

2) A predictive algorithm for ISC quantification was then developed by comparing the *in-situ* ISC values to the reflectance values of the Rayleigh and aerosol-corrected imagery from (1) and finding the line of best fit which was the exponential function

$$y = 1.5559e^{46.641x}$$

where ‘x’ is the Rayleigh and aerosol corrected reflectance (R (%/100)) and ‘y’ is the estimate of sediment concentration (mg L^{-1}). The algorithm was developed specifically for high concentrations of sediment up to 300 mg L^{-1}. The newly developed Lake Pontchartrain predictive sediment algorithm performed well in hind-casting surface suspended sediment concentrations for the selected 2016 BCS diversion images, with an RMSE value of 25.77 (mg L^{-1}). This error value is similar to other MODIS remote sensing studies of high sediment concentration (Chen et al. 2015; Kaba et al. 2014; Qiu 2013).

3) The ISC algorithm developed in (2) was successfully used to track Mississippi River sediment plume motion throughout the 2016 BCS diversion as well as to map suspended sediment distributions well after the Spillway closure. To accomplish this, twenty Aqua MODIS images from 11 January to 27 February were selected for analysis. Close inspection of the produced imagery afforded insight into the potential effects of Coriolis, daily winds, and BCS and tributary discharge on the movement of the Mississippi River sediment plume.

4) Comparison of sequences of clear-sky MODIS images yielded an understanding of the wind direction’s potential to influence the location of the highest concentration of Mississippi River sediment within Lake Pontchartrain. It was more difficult to determine to what degree wind speed played a role in resuspension of sediment although at least three ranges of dates showed increased plume size and mean concentration after periods of increased winds. Similarly, a major reduction in wind speed was followed by a reduction in plume area and mean concentration on at least one occasion. Reliable wind estimates for Lake Pontchartrain would be greatly aided by the addition of wind stations along the Causeway. The wind data from the NDBC stations did not appear to agree fully with field observations of wind speeds and it is

unknown to what degree the MSY station wind data is representative of Lake conditions given its distance from the Lake (~8 km).

5) The time-series of MODIS imagery did provide unique insight into the apparent repeated resuspension of Mississippi River sediment both during the BCS diversion and in the month timeframe following its closure.

While this study demonstrates the benefits of using satellite remote sensing for large spatial scale observations and quantification of oceanographic variables, the research could have been improved in a number of ways. Firstly, the majority of discarded *in-situ* sediment data were not usable because they were not collected near enough to the time of the satellite image collection. *In-situ* data collection should be conducted as near to satellite image collection time as possible because of the rapidly changing surface conditions especially during a BCS diversion event. Miller and McKee (2004) suggest only using *in-situ* data collected within 30 minutes of MODIS satellite image collection time. Furthermore, data samples were collected only from the western half of the Lake, west of the Causeway bridge, so future studies may benefit from *in-situ* data collection at a wider range of locations. An enhanced understanding of the sedimentary characteristics, chemical compositions, and spectral behavior of Mississippi River material prevalent in the Lake during diversion events would help refine satellite algorithms even further. Algorithm development would benefit from the addition of field measurements of absorption from CDOM and organic sediments, and absorption and/or fluorescence from chlorophyll *a*. Collection of water samples at various depths in the water column could provide insight as to what degree stratification and resuspension may be affected by winds. While wind direction helped to explain the location of the highest areas of sediment concentration, more detailed modeling of winds in concert with bathymetry, water column stratification, tides, tributary

discharge, and sediment composition, among other meteorological and oceanographic mechanisms, would be helpful in future research on the Mississippi River sediment plume concentration and resuspension variability.

REFERENCES

Abernethy, Y., and Turner, R. E., (1987). United States forested wetlands - 1940-1980. Bioscience 37(10): 721-727.

Allen, Y., Couvillion, B., and Barra, J., (2012). Using multitemporal remote sensing imagery and inundation measures to improve land change estimates in coastal wetlands. Estuaries and Coasts 35(1): 190-200.

APHA, (2005). Standard methods for the examination of water and wastewater. Eaton, A., Clesceri, L., Rice, E., and Greenberg, A. (eds.), American Public Health Association 21(2): 58-59.

Antoine, D., Morel, A., Gentili, B., Gordon, H. R., Banzon, V. F., Evans, R. H., Brown, J.W., Walsh, S., Baringer, W., and Li, A., (2003). In search of long-term trends in ocean color. Eos, Transactions American Geophysical Union 84(32): 301-309.

Barber, R. T. and A. K. Hilting (2000). Achievements in biological oceanography. http://www.ncbi.nlm.nih.gov/books/NBK208835/

Bargu, S., White, J. R., Li, C. Y., Czubakowski, J., and Fulweiler, R. W., (2011). Effects of freshwater input on nutrient loading, phytoplankton biomass, and cyanotoxin production in an oligohaline estuarine lake. Hydrobiologia 661(1): 377-389.

Barnes, S., Bond, C., Burger, N., Anania, K., Strong, A., Weilant, S., and Virgets, S., (2015). Economic evaluation of coastal land loss in Louisiana. LSU Economics & Policy Research Group.

Barnes, S., Terrell, D., Virgets, S., and Vincent, B., (2016). Connection to the coast: Linking commercial fishing activity to coastal communities. Coastal Protection and Restoration Authority.

Barnes, W. L., Pagano, T.S., Salomonson V.V., (1998). Prelaunch characteristics of the Moderate Resolution Imaging Spectroradiometer (MODIS) on EOS-AM1. IEEE Transactions on Geoscience and Remote Sensing 36(4): 1088-1100.

Barry, J. M., (1997). Rising tide: the Great Mississippi Flood of 1927 and how it changed America. New York: Simon & Shuster. Print.

Booth, J. G., Miller, R. L., McKee, B. A., and Leathers, R. A. (2000). Wind-induced bottom sediment resuspension in a microtidal coastal environment. Continental Shelf Research 20(7): 785-806.

Burkart, M. R. and James, D. E. (1999). Agricultural-nitrogen contributions to hypoxia in the Gulf of Mexico. Journal of Environmental Quality 28(3): 850-859.

Chen, S., Han, L., Chen, X., Li, D., Sun, L., and Li, Y., (2015) Estimating wide range total suspended solids concentrations from MODIS 250-m imageries: An improved method. ISPRS Journal of Photogrametry and Remote Sensing 99: 58–69.

Costa, P. R. (2016). Impact and effects of paralytic shellfish poisoning toxins derived from harmful algal blooms to marine fish. Fish and Fisheries 17(1): 226-248.

Dash, P., Walker, N., D., Mishra, D. R., Hu, C., Pinckney, J. L., and D'Sa, E. J., (2011). Estimation of cyanobacterial pigments in a freshwater lake using OCM satellite data. Remote Sensing of Environment 115(12): 3409-3423.

Day, J., Lane, R., Mach, R., Brantley, C., Daigle, M., (1999). Water chemistry dynamics in Lake Pontchartrain, Louisiana, during the 1997 opening of the Bonnet Carre Spillway. Recent Research in Coastal Louisiana: Natural System Function and Response to Human Influence: 89-100.

de Magalhaes, V. F., Soares, R. M., and Azevedo, S., (2001). Microcystin contamination in fish from the Jacarepagua Lagoon (Rio de Janeiro, Brazil): Ecological implication and human health risk. Toxicon 39(7): 1077-1085.

Eadie, B. J., McKee, B. A., Lansing, M. B., Robbins, J. A., Metz, S., and Trefry, J. H. (1994). Records of nutrient-enhanced coastal ocean productivity in sediments from the Louisiana continental-shelf." Estuaries 17(4): 754-765.

Elliot, D. (1932). The improvement of the lower Mississippi river for flood control and navigation. St. Louis, Mo., M.R.C. Print.

Goolsby, D. A., and Battaglin W. A., (2001). Long-term changes in concentrations and flux of nitrogen in the Mississippi River Basin, USA. Hydrological Processes 15(7): 1209-1226.

Gordon, H. R., (1978). Removal of atmospheric effects from satellite imagery of the oceans. Applied Optics 17(10): 1631-1636.

Gordon, H. R., Brown, J. W., and Evans, R. H., (1988). Exact rayleigh-scattering calculations for use with the Nimbus-7 coastal zone color scanner. Applied Optics 27(5): 862-871.

Gordon, H. R., and Wang M. H., (1994). "Retreival of water-leaving radiance and aerosol optical-thickness over the oceans with SeaWiFS - a preliminary algorithm. Applied Optics 33(3): 443-452.

Gordon, H. R. (1997). "Atmospheric correction of ocean color imagery in the Earth Observing System era." Journal of Geophysical Research-Atmospheres 102(D14): 17081-17106.

Hovis, W. A., Clark, D. K., Anderson, F., Austin, R. W., Wilson, W. H., Baker, E. T., Ball, D., Gordon, H. R., Mueller, J. L., El-Sayed, S. Z., Sturm, B., Wrigley, R. C., and Yentsch, C. S., (1980). Nimbus-7 coastal zone color scanner: system description and initial Imagery." Science 210(4465): 60.

Howarth, R. W., Sharpley, A., and Walker, D., (2002). Sources of nutrient pollution to coastal waters in the United States: Implications for achieving coastal water quality goals. Estuaries 25(4B): 656-676.

Hu, C. M., Carder, K. L., and Muller-Karger, F. E., (2000). Atmospheric correction of SeaWiFS imagery over turbid coastal waters: A practical method. Remote Sensing of Environment 74(2): 195-206.

Hu, C., Chen, Z., Clayton, T. D., Swarzenski, P., Brock, J. C., and Muller–Karger, F. E., (2004). Assessment of estuarine water-quality indicators using MODIS medium-resolution bands: Initial results from Tampa Bay, FL. Remote Sensing of Environment 93(3): 423-441.

IOCCG, (1999). Status and plans for satellite ocean colour mission: considerations for complementary missions. Yoder, J.A. (ed.), Reports of the International Ocean-Colour Coordinating Group, No. 2, IOCCG, Dartmouth, N.S., Canada.

IOCCG, (2014a). CZCS: Coastal Zone Colour Scanner. http://www.ioccg.org/sensors/czcs.html.

IOCCG, (2014b). SeaWiFS: Sea-viewing Wide Field-of-view Sensor. http://www.ioccg.org/sensors/seawifs.html.

Jadwin, M. G. E., (1927). Flood control in the Mississippi Valley. U. S. Congress H. Rep. No. 70-90.

Justic, D., Rabalais, N. N., Turner, R. E., and Wiseman, W. J. (1993). Seasonal coupling between riverborne nutrients, net producticity and hypoxia. Marine Pollution Bulletin 26(4): 184-189.

Kaba, E., Philpot,W., and Steenhuis, T., (2014) Evaluating suitability of MODIS-Terra images for reproducing historic sediment concentrations in water bodies: Lake Tana, Ethiopia. International Journal of Applied Earth Observation and Geoinformation 26: 286–297.

Kolic, P. E., Roy, E. D., White, J. R., and Cook, R. L., (2014). Spectroscopic measurements of estuarine dissolved organic matter dynamics during a large-scale Mississippi River flood diversion. Science of The Total Environment 485–486: 518-527.

Lake Pontchartrain Basin Foundation – LPBF, (2016). History of the Pontchartrain Basin http://www.saveourlake.org/basin-history.php

Lee, Z., Carder, K. L., Steward, R. G., Peacock, T. G., Davis, C. O., and Mueller, J. L., (1997). Remote sensing reflectance and inherent optical properties of oceanic waters derived from above-water measurements. SPIE Proceedings 2963: 160-166

Lynch, P. (2011). The end of a remarkable mission: SeaWiFS' thirteen years of observing our home planet. http://www.nasa.gov/topics/earth/features/seawifs_end.html.

Manganelli, M. (2016). Blooms of toxic microorganisms in aquatic environments: Marine microalgae and freshwater cyanobacteria. A brief review with a particular focus on the Italian

situation diffusion and health effects of toxic marine microalgae and freshwater cyanobacteria in Italy. Rendiconti Lincei-Scienze Fisiche E Naturali 27(1): 135-143.

McCorquodale, J. A., Roblin, R. J., Georgiou, I. Y., and Haralampides, K. A., (2009). Salinity, nutrient, and sediment dynamics in the Pontchartrain Estuary. Journal of Coastal Research: 71-87.

Miller, R. L., and McKee, B. A., (2004). Using MODIS Terra 250 m imagery to map concentrations of total suspended matter in coastal waters. Remote Sensing of Environment 93(1–2): 259-266.

Mize, S. V., and Demcheck, D. K., (2009). Water quality and phytoplankton communities in Lake Pontchartrain during and after the Bonnet Carré Spillway opening, April to October 2008, in Louisiana, USA. Geo-Marine Letters 29(6): 431-440.

Mobley, C. D. (1999). Estimation of the remote-sensing reflectance from above-surface measurements. Applied Optics 38(36): 7442-7455.

Morel, A., and Prieur, L., (1977). Analysis of variations in ocean color. Limnology and Oceanography 22(4): 709-722.

Morel, A., and Gentili, B., (1993). Diffuse reflectance of oceanic waters. Applied Optics 32: 6864-6872.

Myint, S. W., and Walker, N. D., (2002). Quantification of surface suspended sediments along a river dominated coast with NOAA AVHRR and SeaWiFS measurements: Louisiana, USA. International Journal of Remote Sensing 23(16): 3229-3249.

NOAA, (2016). NOAA Satellite Information System. http://noaasis.noaa.gov/NOAASIS/ml/40yearsa.html

OBPG, (2014). Product Definitions. https://oceancolor.gsfc.nasa.gov/cms/products

Ogburn, M. B., Jackson, J. L., and Forward, R. B., (2007). Comparison of low salinity tolerance in Callinectes sapidus Rathbun and Callinectes similis Williams postlarvae upon entry into an estuary. Journal of Experimental Marine Biology and Ecology 352(2): 343-350.

Park, E. and Latrubesse, E. M., (2014). Modeling suspended sediment distribution patterns of the Amazon River using MODIS data. Remote Sensing of Environment 147, 232-242.

Qiu, Z., (2013) A simple optical model to estimate suspended particulate matter in Yellow River Estuary. Optics Express 21: 27891–27904.

Rabalais, N. N., Turner, R.E., Wiseman, W.J., and Boesch, D.F., (1991). A brief summary of hypoxia on the northern Gulf of Mexico continental shelf: 1985–1988. In R. V. Tyson and T. H. Pearson (eds.), Modern and Ancient Continental Shelf Anoxia, Geological Society Special Publication, The Geological Society, London, England. 58: 35-47.

Rabalais, N. N., (2015). Human impacts on fisheries across the land-sea interface. Proceedings of the National Academy of Sciences of the United States of America 112(26): 7892-7893.

Ramatchandirane, C.G, Allison, M.A., Walker, N.D, Haag, A.S., Yuill, B.T., Baustian, M.M., Meselhe, E.A., Joshi, I.D., Effects of a Mississippi River diversion on suspended sediment and salinities in Barataria Basin, Louisiana, from 2009 to 2015, Estuarine, Coastal and Shelf Science, in preparation.

Robinson, I. S. (2004). Measuring the Oceans from Space: The principles and methods of satellite oceanography.

Roy, E. D., White, J. R., Smith, E. A., Bargu, S., and Li, C. Y., (2013). Estuarine ecosystem response to three large-scale Mississippi River flood diversion events. Science of The Total Environment 458: 374-387.

Sikora, W. B., and Kjerfve, B., (1985). Factors influencing the salinity regime of Lake Pontchartrain, Louisiana, a shallow coastal lagoon - analysis of a long-term data set. Estuaries 8(2A): 170-180.

Siegel, D. A., Wang, M. H., Maritorena, S., and Robinson, W. (2000). Atmospheric correction of satellite ocean color imagery: The black pixel assumption. Applied Optics 39(21): 3582-3591.

Stumpf, R. P., and Goldschmidt, P. M., (1992). Remote-sensing of suspended sediment discharge into the Western Gulf of Maine during the April 1987 100-year flood. Journal of Coastal Research 8(1): 218-225.

Turner, R. E., Dortch, Q., and Rabalais, N.N., (2004). Inorganic nitrogen transformations at high loading rates in an oligohaline estuary. Biogeochemistry 68(3): 411-423.

Turner, R. E., and Rabalais N. N., (1991). "Changes in Mississippi River water-quality this century." Bioscience 41(3): 140-147.

Turner, R. E., and Rabalais, N. N., (1994). Coastal eutrophication near the Mississippi River Delta. Nature 368(6472): 619-621.

USACE, (2016). Bonnet Carré Spillway operational effects. http://www.mvn.usace.army.mil/Missions/MississippiRiverFloodControl/BonnetCarreSpillwayOverview/SpillwayOperationInformation.aspx.

USGS, (2005). Largest Rivers in the United States.

USGS, NOAA, and National Atlas of the United States of America, (2003). Great Lakes.

Walker, N. D., (1996). Satellite assessment of Mississippi River plume variability: Causes and predictability. Remote Sensing of Environment 58(1): 21-35.

Walker, N. D., and Hammack, A.B., (2000). Impacts of winter storms on circulation and sediment transport: Atchafalaya-Vermilion Bay Region, Louisiana, U.S.A. Journal of Coastal Research 16(4): 996-1010.

Walker, N.D. (2001). Tropical and extra-tropical storm impacts on circulation, sediment and salt flux: Atchafalaya-Vermilion Bay region, Louisiana coast. Estuaries 24: 498-508.

Walker, N., Myint, S., Babin, A., and Haag, A, (2003). Advances in satellite radiometry for the surveillance of surface temperatures, ocean eddies and upwelling processes in the Gulf of Mexico using GOES-8 measurements during summer. Geophysical Research Letters 30(16): 4.

Walker, N.D., and Rabalais, N.N., (2006). Relationships among satellite chlorophyll a, river inputs and hypoxia on the Louisiana continental shelf, Gulf of Mexico. Estuaries and Coasts 9 (6b); 1-13.

Walker, N., Pilley, C., Raghunathan, V., D'Sa, E., Leben, R., Hoffman, N., Brickley, P., Coholan, P., Sharma, N., Graber, H., and Turner, R. (2011). Impacts of loop current frontal cyclonic eddies and wind forcing on the 2010 Gulf of Mexico Oil Spill. Geophysical Monograph Series: 103-116.

Wang, H., Hladik, C. M., Huang, W., Milla, K., Edmiston, L., Harwell, M. A., and Schalles, J. F. (2010). Detecting the spatial and temporal variability of chlorophyll-a concentration and total suspended solids in Apalachicola Bay, Florida using MODIS imagery. International Journal of Remote Sensing 31(2): 439-453.

Wang, M. H., Shi, W., and Jiang, L. D. (2012). Atmospheric correction using near-infrared bands for satellite ocean color data processing in the turbid western Pacific region. Optics Express 20(2): 741-753.

White, J. R., Fulweiler, R. W., Li, C. Y., Bargu, S., Walker, N. D., Twilley, R. R., and Green, S. E., (2009). Mississippi River Flood of 2008: Observations of a large freshwater diversion on physical, chemical, and biological characteristics of a shallow estuarine lake. Environmental Science & Technology 43(15): 5599-5604.

Wiseman, W. J., Rabalais, N.N., Turner, R.E., Dinnel, S.P., and MacNaughton, A., (1997). Seasonal and interannual variability within the Louisiana coastal current: Stratification and hypoxia. Journal of Marine Systems 12: 237–248.

Zhao, H. H., Chen, Q., Walker, N. D., Zheng, Q. A., and MacIntyre, H. L. (2011). A study of sediment transport in a shallow estuary using MODIS imagery and particle tracking simulation. International Journal of Remote Sensing 32(21): 6653-6671.

APPENDIX A: *IN-SITU* SEDIMENT DATA

Table A.1: *In-situ* water sample analysis with Unique ID corresponding to Figures 5.2 and 5.3

Unique ID	Date	Time (UTC)	Station	Suspended Sediment (mg L^{-1})	Inorganic Sediment (mg L^{-1})	Latitude	Longitude
1	1/15/2016	1650	13	53.93	42.70	30.106	-90.319
2	1/15/2016	1638	14	33.81	27.05	30.122	-90.291
3	1/15/2016	1629	15	11.32	7.55	30.138	-90.263
4	1/15/2016	1619	16	11.76	8.82	30.159	-90.228
5	1/23/2016		1	307.50	267.81	30.071	-90.148
6	1/23/2016		1	322.50	281.00	30.071	-90.148
7	1/23/2016		1	303.10	267.64	30.071	-90.148
8	1/23/2016		1	313.00	275.00	30.071	-90.148
9	1/23/2016		2	198.61	172.31	30.128	-90.139
10	1/23/2016		2	235.83	206.25	30.128	-90.139
11	1/23/2016		2	225.15	197.36	30.128	-90.139
12	1/23/2016		3	88.52	77.87	30.200	-90.127
13	1/23/2016		3	90.47	78.21	30.200	-90.127
14	1/23/2016		3	89.73	79.26	30.200	-90.127
15	1/23/2016		4	70.80	60.58	30.257	-90.115
16	1/23/2016		4	72.43	61.75	30.257	-90.115
17	1/23/2016		4	67.78	58.85	30.257	-90.115
18	1/23/2016		5	42.66	35.71	30.314	-90.106
19	1/23/2016		5	41.62	35.50	30.314	-90.106
20	1/23/2016		5	41.49	36.40	30.314	-90.106
21	1/24/2016		11	78.26	66.67	30.081	-90.363
22	1/24/2016		12	54.84	48.39	30.091	-90.344
23	1/24/2016		13	57.63	44.07	30.106	-90.319
24	1/24/2016		14	51.85	44.44	30.122	-90.291
25	1/24/2016	1735	15	81.82	59.09	30.138	-90.263
26	1/24/2016		16	160.00	137.14	30.159	-90.228
27	1/24/2016		17	160.55	128.44	30.177	-90.198
28	1/24/2016		18	103.98	76.45	30.196	-90.164
29	1/29/2016	1725	11	44.74	31.58	30.081	-90.363
30	1/29/2016	1715	12	34.69	22.45	30.091	-90.344
31	1/29/2016	1707	13	16.28	6.98	30.106	-90.319
32	1/29/2016	1653	14	28.57	21.43	30.122	-90.291
33	1/29/2016	1645	15	42.11	28.95	30.138	-90.263

Table A.1 Continued

Unique ID	Date	Time (UTC)	Station	Suspended Sediment (mg L^{-1})	Inorganic Sediment (mg L^{-1})	Latitude	Longitude
34	1/29/2016	1634	16	30.09	21.24	30.159	-90.228
35	1/29/2016	1624	17	8.20	3.28	30.177	-90.198
36	1/29/2016	1615	18	8.33	0.00	30.196	-90.164
37	2/5/2016	1832	11	84.62	61.54	30.081	-90.363
38	2/5/2016	1823	12	71.43	53.57	30.091	-90.344
39	2/5/2016	1815	13	50.00	38.24	30.106	-90.319
40	2/5/2016	1801	14	44.19	32.56	30.122	-90.291
41	2/5/2016	1748	15	39.22	29.41	30.138	-90.263
42	2/5/2016	1737	16	29.51	22.95	30.159	-90.228
43	2/5/2016	1727	17	12.94	8.24	30.177	-90.198
44	2/5/2016	1717	18	6.17	2.47	30.196	-90.164
45	2/19/2016	1728	11	29.74	25.64	30.081	-90.363
46	2/19/2016	1712	12	25.27	21.98	30.091	-90.344
47	2/19/2016	1705	13	18.27	15.38	30.106	-90.319
48	2/19/2016	1642	15	11.46	8.33	30.138	-90.263
49	2/19/2016	1630	16	12.00	9.00	30.159	-90.228
50	2/19/2016	1620	17	11.00	9.00	30.177	-90.198
51	2/19/2016		18	3.11	1.04	30.196	-90.164
52	2/26/2016		11	73.08	53.85	30.081	-90.363
53	2/26/2016		12	107.14	71.43	30.091	-90.344
54	2/26/2016		13	135.71	100.00	30.106	-90.319
55	2/26/2016		14	126.32	94.74	30.122	-90.291
56	2/26/2016		15	114.29	85.71	30.138	-90.263
57	2/26/2016		16	76.92	58.97	30.159	-90.228
58	2/26/2016		17	64.00	50.00	30.177	-90.198
59	3/13/2016	1809	1	41.80	35.60	30.072	-90.233
60	3/13/2016	1841	2	41.70	35.37	30.108	-90.235
61	3/13/2016	1909	3	46.70	38.74	30.142	-90.234
62	3/13/2016	1936	4	39.90	33.44	30.179	-90.197
63	3/13/2016	1954	5	52.70	43.81	30.237	-90.250
64	3/13/2016	2024	6	82.90	72.00	30.293	-90.302
65	3/13/2016	2043	7	59.90	50.80	30.230	-90.303
66	3/13/2016	2113	8	35.90	30.02	30.122	-90.291
67	3/25/2016		11	35.71	26.19	30.081	-90.363
68	3/25/2016		12	31.91	23.40	30.091	-90.344

Table A.1 Continued

Unique ID	Date	Time (UTC)	Station	Suspended Sediment (mg L^{-1})	Inorganic Sediment (mg L^{-1})	Latitude	Longitude
70	3/25/2016		14	32.88	19.18	30.122	-90.291
71	3/25/2016		15	57.14	39.29	30.138	-90.263
72	3/25/2016		16	67.86	50.00	30.159	-90.228
73	3/25/2016		17	47.37	34.21	30.177	-90.198
74	3/25/2016		18	46.34	34.15	30.196	-90.164

APPENDIX B: INORGANIC SEDIMENT ALGORITHM DEVELOPMENT DATA

Table B.1: *In-situ* water samples and their associated red band (645 nm) reflectance values

Unique ID	Date	Station	Inorganic Sediment (mg L^{-1})	Latitude	Longitude	Aerosol-corrected Reflectance	Rayleigh-corrected Reflectance
5	1/23/2016	1	267.81	30.071	-90.148	0.10640312	0.1087031
6	1/23/2016	1	281.00	30.071	-90.148	0.10640312	0.1087031
7	1/23/2016	1	267.64	30.071	-90.148	0.10640312	0.1087031
8	1/23/2016	1	275.00	30.071	-90.148	0.10640312	0.1087031
9	1/23/2016	2	172.31	30.128	-90.139	0.10311224	0.1054122
10	1/23/2016	2	206.25	30.128	-90.139	0.10311224	0.1054122
11	1/23/2016	2	197.36	30.128	-90.139	0.10311224	0.1054122
12	1/23/2016	3	77.87	30.200	-90.127	0.09004008	0.0923401
13	1/23/2016	3	78.21	30.200	-90.127	0.09004008	0.0923401
14	1/23/2016	3	79.26	30.200	-90.127	0.09004008	0.0923401
15	1/23/2016	4	60.58	30.257	-90.115	0.07858276	0.0808828
16	1/23/2016	4	61.75	30.257	-90.115	0.07858276	0.0808828
17	1/23/2016	4	58.85	30.257	-90.115	0.07858276	0.0808828
18	1/23/2016	5	35.71	30.314	-90.106	0.06522883	0.0675288
19	1/23/2016	5	35.50	30.314	-90.106	0.06522883	0.0675288
20	1/23/2016	5	36.40	30.314	-90.106	0.06522883	0.0675288
52	2/26/2016	11	53.85	30.081	-90.363	0.08384927	0.0938493
53	2/26/2016	12	71.43	30.091	-90.344	0.090518	0.100518
54	2/26/2016	13	100.00	30.106	-90.319	0.09022468	0.1002247
55	2/26/2016	14	94.74	30.122	-90.291	0.08640172	0.0964017
56	2/26/2016	15	85.71	30.138	-90.263	0.07965946	0.0896595
57	2/26/2016	16	58.97	30.159	-90.228	0.07577381	0.0857738
58	2/26/2016	17	50.00	30.177	-90.198	0.07763496	0.087635
75	4/5/2016	BB1				0.03635	
76	4/5/2016	BB2				0.03474	
77	4/5/2016	BB3				0.03491	
78	4/5/2016	BB4				0.02913	
79	4/5/2016	BB5				0.02567	
80	4/5/2016	BB6				0.02289	
81	4/5/2016	BB7				0.021511	
82	4/5/2016	BB8				0.01708	
83	4/5/2016	BB9				0.01629	
84	4/5/2016	BB10				0.01513	
85	4/5/2016	BB11				0.01996	

APPENDIX C: INORGANIC SEDIMENT ALGORITHM VALIDATION

Table C.1: *In-situ* water sample data, algorithm-estimated values, and validation data

Unique ID	Date	Station	In-situ Inorganic Sediment (mg L^{-1})	Algorithm-output Inorganic Sediment (mg L^{-1})	Difference	RMSE
5	1/23/2016	1	267.81	222.47	45.34	25.77
6	1/23/2016	1	281.00	222.47	58.53	
7	1/23/2016	1	267.64	222.47	45.16	
8	1/23/2016	1	275.00	222.47	52.53	
9	1/23/2016	2	172.31	190.82	-18.51	
10	1/23/2016	2	206.25	190.82	15.43	
11	1/23/2016	2	197.36	190.82	6.55	
12	1/23/2016	3	77.87	103.71	-25.84	
13	1/23/2016	3	78.21	103.71	-25.50	
14	1/23/2016	3	79.26	103.71	-24.45	
15	1/23/2016	4	60.58	60.78	-0.19	
16	1/23/2016	4	61.75	60.78	0.97	
17	1/23/2016	4	58.85	60.78	-1.93	
18	1/23/2016	5	35.71	32.60	3.11	
19	1/23/2016	5	35.50	32.60	2.90	
20	1/23/2016	5	36.40	32.60	3.80	
52	2/26/2016	11	53.85	77.70	-23.85	
53	2/26/2016	12	71.43	106.05	-34.62	
54	2/26/2016	13	100.00	104.61	-4.61	
55	2/26/2016	14	94.74	87.52	7.21	
56	2/26/2016	15	85.71	63.91	21.81	
57	2/26/2016	16	58.97	53.32	5.66	
58	2/26/2016	17	50.00	58.15	-8.15	

APPENDIX D: TOTAL LAKE PONTCHARTRAIN SEDIMENT CONCENTRATION

Table D.1: Overall estimated Lake Pontchartrain inorganic sediment concentration (mg L^{-1})

Date	Mean (mg L^{-1})	Max (mg L^{-1})	Min (mg L^{-1})
11-Jan	25	141	4
13-Jan	24	333	3
16-Jan	23	172	3
17-Jan	28	123	3
18-Jan	56	294	3
19-Jan	56	239	3
23-Jan	96	234	6
24-Jan	105	296	5
28-Jan	105	295	5
29-Jan	118	281	5
5-Feb	84	234	6
7-Feb	75	287	7
8-Feb	63	126	20
10-Feb	114	244	14
11-Feb	133	319	41
17-Feb	36	103	9
18-Feb	57	161	14
25-Feb	108	203	13
26-Feb	77	164	10
27-Feb	85	161	15

VITA

Robert Lee Iles IV ("Robbie") was born in Slidell, Louisiana, in 1989, and graduated from Northshore High School in 2007, where he was a National Merit semi-finalist. He received his Bachelor of Science (B.S.) degree in geography from Louisiana State University (LSU) in 2012. Mr. Iles enrolled in the Master of Science (M.S.) program in the LSU Department of Oceanography and Coastal Sciences (DOCS) in 2013 and accepted a position as a GIS analyst at the LSU Stephenson Disaster Management Institute (SDMI) that same year. He left school to work full-time in GIS until 2016, at which time he re-enrolled in DOCS. His research involved satellite remote sensing techniques and application for coastal Louisiana waters. He is expecting to receive his M.S. in Oceanography in the Spring of 2017. After graduation, he will return to SDMI as a Research Associate to explore topics relevant to the science of coastal Louisiana while also contemplating future Doctor of Philosophy (Ph.D.) opportunities.